Planetary and Space Science 73 (2012) 98–118

Contents lists available at SciVerse ScienceDirect

Planetary and Space Science

journal homepage: www.elsevier.com/locate/pss

Density of asteroids

B. Carry *

European Space Astronomy Centre, ESA, P.O. Box 78, 28691 Villanueva de la Cañada, Madrid, Spain

ARTICLE INFO

Article history:
Received 23 August 2011
Received in revised form
1 March 2012
Accepted 6 March 2012
Available online 3 April 2012

Keywords:
Minor planets
Mass
Volume
Density
Porosity

ABSTRACT

The small bodies of our solar system are the remnants of the early stages of planetary formation. A considerable amount of information regarding the processes that occurred during the accretion of the early planetesimals is still present among this population. A review of our current knowledge of the density of small bodies is presented here. Density is indeed a fundamental property for the understanding of their composition and internal structure. Intrinsic physical properties of small bodies are sought by searching for relationships between the dynamical and taxonomic classes, size, and density. Mass and volume estimates for 287 small bodies (asteroids, comets, and transneptunian objects) are collected from the literature. The accuracy and biases affecting the methods used to estimate these quantities are discussed and best-estimates are strictly selected. Bulk densities are subsequently computed and compared with meteorite density, allowing to estimate the macroporosity (*i.e.*, amount of voids) within these bodies. Dwarf-planets apparently have no macroporosity, while smaller bodies (<400 km) can have large voids. This trend is apparently correlated with size: C- and S-complex asteroids tend to have larger density with increasing diameter. The average density of each Bus-DeMeo taxonomic classes is computed (DeMeo et al., 2009; Icarus 202). S-complex asteroids are more dense on average than those in the C-complex that in turn have a larger macroporosity, although both complexes partly overlap. Within the C-complex asteroids, B-types stand out in albedo, reflectance spectra, and density, indicating a unique composition and structure. Asteroids in the X-complex span a wide range of densities, suggesting that many compositions are included in the complex. Comets and TNOs have high macroporosity and low density, supporting the current models of internal structures made of icy aggregates. Although the number of density estimates sky-rocketed during last decade from a handful to 287, only a third of the estimates are more precise than 20%. Several lines of investigation to refine this statistic are contemplated, including observations of multiple systems, 3-D shape modeling, and orbital analysis from Gaia astrometry.

1. Small bodies as remnants of planetesimals

The small bodies of our solar System are the left-overs of the building blocks that accreted to form the planets, some 4.6 Gyr ago. They represent the most direct witnesses of the conditions that reigned in the proto-planetary nebula (Bottke et al., 2002a). Indeed, terrestrial planets have thermally evolved and in some cases suffered erosion (*e.g.*, plate tectonic, volcanism) erasing evidence of their primitive composition. For most small bodies, however, their small diameter limited the amount of radiogenic nuclides in their interior, and thus the amount of energy for internal heating. The evolution of small bodies is therefore mainly exogenous, through eons of collisions, external heating, and bombardment by high energy particles.

A detailed study of the composition of small bodies can be achieved in the laboratory, by analyzing their terrestrial counterparts: meteorites. The distribution of elements, isotopes in meteorites, together with the level of heating and aqueous alteration they experienced tell us about the temperature, elemental abundance, and timescales during the accretion stages (*e.g.*, Halliday and Kleine, 2006). The connection of this information with specific locations in the Solar System constrains the formation scenarios of our Solar System. This requires the identification of links between the meteorites and the different populations of small bodies.

Indeed, if meteorites are samples from the Solar System, several questions are raised. Is this sampling complete? Is this sampling homogeneous? Some of the identified asteroid types (see Section 2) lack of a terrestrial analog. The most flagrant examples are the O-type asteroids (3628) Božněmcová and (7472) Kumakiri that appear unlike any measured meteorite assemblage (Burbine et al., 2011). Coupled mineralogical and dynamical studies have shown that meteorites come from specific locations.

* Tel.: +34 91 81 31 233.
E-mail address: benoit.carry@esa.int

0032-0633/$ - see front matter © 2012 Elsevier Ltd. All rights reserved.
http://dx.doi.org/10.1016/j.pss.2012.03.009

Other regions of the Solar System may therefore be unrepresented in our meteorite collection (see the discussions in, Burbine et al., 2002; Bottke et al., 2002b; Vernazza et al., 2008, for instance).

Additionally, the current orbits of small bodies may be different from the place they originally formed. For instance, it has been suggested that the giant planets migrated to their current orbits (the Nice model, see, Tsiganis et al., 2005), injecting material from the Kuiper Belt into the inner Solar System (Levison et al., 2009). Similarly, gravitational interaction among planetary embryos may have caused outward migration of planetesimals from Earth's vicinity into the main belt (Bottke et al., 2006). Current distribution of small bodies may therefore not reflect the original distribution of material in the Solar System. It however tells us about the dynamical processes that occurred over history. Analysis of the composition of meteorites in the laboratory, of small bodies from remote-sensing, and of their distribution in the Solar System are therefore pre-requisites to understanding the formation and evolution of our Solar System.

2. Linking small bodies with meteorites

Most of our knowledge on the mineralogy of asteroids has been derived by the analysis of their reflectance spectra in the visible and near-infrared (VNIR). The shape of these spectra has been used to classify the asteroids into broad groups, following several classification schemes called taxonomies. In what follows, I refer to the taxonomy by DeMeo et al. (2009), based on the largest wavelength range (0.4−2.4 μm). It encloses 15 classes grouped into three *complexes* (C, S, and X), with nine additional classes called *end-members* (see, DeMeo et al., 2009, for a detailed description of the classes). Mineralogical interpretations and links with meteorites have been proposed for several classes.

Asteroids belonging to the S-complex (S, Sa, Sq, Sr, and Sv) and to the Q class have been successfully linked to the most common meteorites, the ordinary chondrites (OCs). This link had been suggested for years based on the presence of two deep absorption bands in their spectra, around 1 and 2 μm, similar to that of OCs and characteristic of a mixture of olivines and pyroxenes (see for instance, Chapman, 1996; Brunetto et al., 2006, among many others). The analysis of the sample from the S-type asteroid Itokawa returned by the Hayabusa spacecraft confirmed this link (Yurimoto et al., 2011). The two end-member classes A and V have a mineralogy related to the S-complex. A-types are asteroids made of almost pure olivine, which possible analogs are the achondrite meteorites of the Brachinite and Pallasite groups (see, *e.g.*, Bell et al., 1989; de León et al., 2004). In opposition, V-types are made of pure pyroxenes and are related to the HED achondrite meteorites (*e.g.*, McCord et al., 1970). A- and V-types are believed to correspond to the mantle and the crust of differentiated parent bodies (Burbine et al., 1996).

The link between the hydrated carbonaceous chondrites (CCs) CI and CM and the asteroids in the C-complex seems well established (Cloutis et al., 2011a,b). The anhydrous CV/CO carbonaceous chondrites have also been linked with B-types (Clark et al., 2010). The scarcity and low contrast of absorption features in the VNIR prevent a detailed description of the mineralogy and association with meteorites of these asteroid types (B, C, Cb, Cg, Cgh, Ch). Spectroscopy in the 2.5−4 μm wavelength range, however, revealed the presence of hydration features (Lebofsky, 1978; Jones et al., 1990; Rivkin et al., 2002). These features were interpreted as evidences for aqueous alteration, similar to that experienced by CI/CM parent bodies (Cloutis et al., 2011a,b). Due to their similar composition to that of the solar photosphere, CI meteorites are often considered the most primitive material in the Solar System (see, Weisberg et al., 2006, for an overview of meteorite classes). This has made the compositional study of these so-called *primitive asteroids* a primary goal in planetary science.

The VNIR spectra of asteroids in the X-complex are devoid of strong absorption bands. However, several weak features (*e.g.*, around 0.9 μm) have been identified and used to discriminate subclasses (Clark et al., 2004; Ockert-Bell et al., 2010; Fornasier et al., 2011). Proposed meteorite analogs for X, Xc, Xe, and Xk asteroids virtually cover the entire meteorite collection: the anhydrous CV/CO carbonaceous chondrites (Barucci et al., 2005, 2012), enstatite chondrites and aubrites (Vernazza et al., 2009b, 2011b; Ockert-Bell et al., 2010), mesosiderites (Vernazza et al., 2009b), stony-iron (Ockert-Bell et al., 2010), and iron meteorites (Fornasier et al., 2011). The mineralogy represented in the X-complex is therefore probably more diverse than in the S- and C-complexes, due to the limits of the taxonomy based on spectral features only. It is worth noting that in former taxonomies (*e.g.*, Tholen and Barucci, 1989), the X-complex was divided into three main groups, E, M, and P, distinguished by albedo.

L-types have been suggested to be the most ancient asteroids that currently exist. From the comparison of their VNIR spectra with laboratory material, a fraction of 30 $\pm$10% of calcium- and aluminum-rich inclusions was proposed (Sunshine et al., 2008). This value is significantly higher than that of meteorites. This suggests a very early accretion together with a low degree of alteration while crossing the entire history of the Solar System. With a similar spectral shape, K-types have often be described as intermediates between S- and C-like material (DeMeo et al., 2009). Most of the K-type are associated with the Eos dynamical family in the outer Main Belt. They have been tentatively linked with the anhydrous CO, CV, and CK, and hydrated but metal-rich CR carbonaceous chondrites meteorites (Bell et al., 1989; Doressoundiram et al., 1998; Clark et al., 2009).

The mineralogy of the remaining end-members classes is more uncertain, owing to the apparent absence of strong spectral features (D and T) or to the mismatch of features with any known material (O and R). It has been suggested that T-types contain a high fraction of metallic contents, and may be related to the iron cores of differentiated asteroids, hence iron meteorites (Britt et al., 1992). D-types are among the reddest objects in the Solar System, not unlike that of comet nuclei and some transneptunian objects (Barucci et al., 2008). Their emission spectra in the mid-infrared indeed show striking similarities with that of comet nuclei (Emery et al., 2006, 2011). Both O and R classes were defined to describe the spectral shape of a single object, (3628) Božněmcová and (349) Dembowska respectively. Both types display broad absorption bands around 1 and 2 μm. These bands are however unlike those of S-types or any type of pyroxenes and olivines in our sample collection (Burbine et al., 2011).

Comets and transneptunian objects (TNOs) are volatile-rich bodies. These two populations are dynamically linked, the latter being one of the reservoir of periodic comets (Jewitt, 2004). Several compositional groups have been identified among TNOs: water ice dominated spectra, methane-rich spectra, and featureless spectra similar to that of comet nuclei (Barucci et al., 2008). There is no evidence for a meteorite sample from these dynamic classes, although the delivery from Kuiper Belt material to Earth should be possible (Gounelle et al., 2008).

As seen from this short summary, asteroid–meteorites connections and detailed mineralogy remain open questions in many cases: only about half of the 24 classes defining the taxonomy by DeMeo et al. (2009) have a mineralogical interpretation. Expanding the taxonomy toward longer wavelengths (2–5 and 5−40 μm range) will help in that respect (*e.g.*, Rivkin et al., 1995, 2002; Emery et al., 2006). Additional constraints must however be used to refine current mineralogy interpretations, especially for objects

with featureless spectra. Visible and radar albedos, thermal inertia, and density provide valuable constraints on the composition of these objects (*e.g.*, Fornasier et al., 2011). Among these, the most fundamental property to understand the composition and internal structure is perhaps the density (Britt et al., 2002; Consolmagno et al., 2008).

3. The density: a fundamental property

As described above, from the analysis of the surface properties such as reflectance spectra or albedo, it is possible to make inferences on composition. These observables however tell us about surface composition only, which may or may not be reflective of the bulk composition of the body (Elkins-Tanton et al., 2011). For instance, the surface of Earth, the *Blue Planet*, is covered by water while its overall composition is totally different. Earth's density is indeed indicative of a rocky composition with a core of denser material. Densities of small bodies are much more subtle, but still contain critical information.

From the compilation of the density of about 20 asteroids, Britt et al. (2002) already showed that differences are visible among that population. In a more recent review including 40 small bodies, Consolmagno et al. (2008) highlighted four trends in macroporosity (hereafter $\mathcal{P}$). The macroporosity reflects the amount of voids larger than the typical micrometer-sized cracks of meteorites. The largest asteroids (mass above 10^{20} kg) are apparently compact bodies without any macroporosity. This contrasts strongly with all the other less massive small bodies that have 20% or more macroporosity. The fraction of voids increases dramatically for icy bodies (comets and TNOs). Finally, *primitive* C-type asteroids tends to have larger macroporosity than the *basaltic* S-type.

Macroporosity, if present to a large extend, may have strong consequences on certain physical properties such as gravity field, thermal diffusivity, seismic velocity, and of course on collisional lifetimes (see the review by Britt et al., 2002). Macroporosity can also help in understanding the collisional history: intact bodies are expected to have low-to-no macroporosity, while heavily impacted objects may have large cracks, fractures (*i.e.*, moderate $\mathcal{P}$), or be gravitational re-accumulation of material (*i.e.*, rubble-piles, characterized by high values of $\mathcal{P}$).

4. Determination of density

Direct measurement of the *bulk* density (ρ) involves the independent measures of the mass (M) and volume (V): $\rho = M/V$. Indirect determination of the density are also possible by modeling the mutual eclipses of a binary system (*e.g.*, Behrend et al., 2006) or the non-gravitational forces on a comet nucleus (*e.g.*, Davidsson et al., 2007). This study aims at deriving constraints on the intrinsic physical properties of small bodies by searching for relationships between the dynamical and taxonomic classes, size, and density. An extensive compilation of the mass, volume, and resulting density estimates available in the literature is therefore presented here.

There are 994 published mass estimates for 267 small bodies (Section 4.1). For each object, the volume determinations are also compiled here, resulting in 1454 independent estimates (Section 4.2). Finally, the density of 24 small bodies has also been indirectly determined (Section 4.3). In total, 287 density estimates are available, for small bodies pertaining to all the dynamical classes: 17 near-Earth asteroids (NEAs), 230 Main-Belt (MBAs) and Trojan asteroids, 12 comets, and 28 transneptunian objects (TNOs). There is however a large spread among the independent estimates of the mass and volume estimates of these objects. Additionally, several estimates lead to obvious non-physical densities such as 0.05 or 20, the respective densities of Aerogel and Platinum. A rigorous selection of the different estimates is therefore needed. Some specifics of mass and diameter estimates are discussed below, together with selection criteria.

4.1. Mass estimates

The determination of the mass of a minor planet relies on the analysis of its gravitational effects on other objects (see the review by Hilton (2002), for instance). The 994 mass estimates for 267 small bodies listed in Appendix A can be divided into four categories, owing to the gravitational effects that were analyzed:

1. *Orbit deflection during close encounters*: The mass of small bodies is several order of magnitude lower than that of planets. Asteroids can nevertheless slightly influence the orbit of other smaller asteroids (*e.g.*, Michalak, 2000, 2001) and of Mars (*e.g.*, Pitjeva, 2001; Mouret et al., 2009) during *close* encounters. This method has been widely used, resulting in 547 mass estimates. An accuracy of few percent can be reached for the most massive asteroids such as (1) Ceres, (2) Pallas, or (4) Vesta (*e.g.*, Konopliv et al., 2006; Zielenbach, 2011). The accuracy however drops for smaller asteroids, and about a third have uncertainties cruder than 100% (see, for instance, Somenzi et al., 2010; Zielenbach, 2011, and Fig. 1a).
2. *Planetary ephemeris*: Numerical models have been developed to describe and predict the position of planets and minor planets around the Sun. In addition to the Sun and the planets, the gravitational influence of several asteroids must be taken into account to properly describe the observed position of planets, satellites, and spacecrafts (see, Baer and Chesley, 2008; Baer et al., 2011; Fienga et al., 2008, 2009, 2010; Folkner et al., 2009, for details). In that respect, this method is similar to the analysis of close encounters. There is however a strong philosophical difference between these two methods: analysis of close encounters consists of considering N times a 1-to-1 gravitational interaction, while planetary ephemeris are conceptually closer to an N-to-1 interaction. Similar to the results obtained from close encounters, the best accuracy is achieved for largest asteroids and becomes cruder for smaller

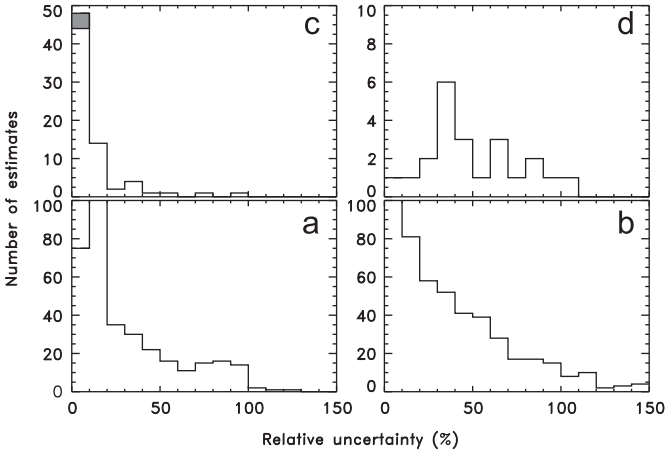

Fig. 1. Distribution of the relative accuracy of mass estimates obtained with four different methods (see text): (a) orbit deflection during close encounters, (b) planetary ephemeris, (c) orbit of natural satellites or spacecrafts (gray bar), and (d) indirect determination of density (Section 4.3) converted into mass.

objects. The mean accuracy is of 45%, but values are distributed up to 100% (Fig. 1b).

3. *Spacecraft tracking*: The Doppler shifts of the radio signals sent by spacecraft around an asteroid can be used to determine its orbit or the deflection of its trajectory during a flyby. These frequency shifts are imposed by the gravitational perturbation and are related to the mass of the asteroid (Yeomans et al., 1997, 2000; Fujiwara et al., 2006; Pätzold et al., 2011). It is by far the most precise technique with a typical accuracy of a couple of percent (Fig. 1c). It will however remain limited to a handful of small bodies (only four to date).
4. *Orbit of a satellite*: From optical or radar images of the components of the system, their mutual orbit can be determined and the mass derived with Kepler's third law (see, for instance, Petit et al., 1997; Merline et al., 1999, 2002; Margot et al., 2002, Marchis et al., 2005, 2008a,b, Brown et al., 2005, 2010; Carry et al., 2011; Fang et al., 2011). The 28 mass estimates available for TNOs were derived from optical imaging with the Hubble space telescope or large ground-based telescopes equipped with adaptive-optics cameras (*e.g.*, Grundy et al., 2009; Dumas et al., 2011). Similarly, the 17 mass estimates for NEAs were all derived from radar (*e.g.*, Ostro et al., 2006; Shepard et al., 2006), with the exception of Itokawa which was the target of the Hayabusa sample-return mission (Fujiwara et al., 2006). Additionally, the mass of 26 MBAs was determined by optical imaging. In total, 68 mass estimates have been derived by analyzing the orbit of a satellite. It is the second most-precise technique with a typical accuracy of about 10–15% (Fig. 1c). It is the most productive method of accurate mass determinations. With currently more than 200 known binaries, many mass estimates are still to come.

Based on these considerations and a close inspection of the different mass estimates available (*e.g.*, Fig. 2), the following criteria for selecting mass estimates were applied: Mass estimates derived from either the third or the fourth method (spacecraft or satellite) prevail upon the first two methods (deflection and ephemeris). Mass estimates leading to non-physical densities are discarded. Mass estimates that do not agree within uncertainties with the range drawn by the weighted average and standard deviation are discarded. The weighted average and standard deviation are subsequently recomputed. The 994 mass estimates are provided in Appendix A together with bibliographic references and notes on selection.

A summary of the precision achieved on mass estimates is presented in Fig. 3. The contribution provided here is illustrated by the difference between the cumulative distribution of relative precision before (dashed line) and after (solid line) the selection (about 20% of the estimates were discarded). For estimates with a relative uncertainty below 50%, the selection of estimates slightly improves the final accuracy, increasing the number of accurate estimates by 5–10%. The apparent *degradation* introduced by the selection for low-precision estimates is due to a rejection of about 10% of these estimates. In other words, these estimates lead to unrealistic densities and should not be considered. Furthermore, the distribution presented in Fig. 3 is based on the uncertainties reported by the different authors. The discrepancy between estimates however often reaches disconcerting levels. For instance, the estimates M_{28} (Krasinsky et al., 2001), M_{72} (Baer et al., 2008), M_{80} (Fienga et al., 2009), and M_{86} (Folkner et al., 2009) of the mass of (52) Europa fall within the range drawn by the weighted mean and deviation (Fig. 2). They nevertheless strongly disagree: the different values are between 4 and 11 σ one from each other.

Such differences are indicative of underestimated uncertainties. Accuracy is often reported as the formal standard deviation (σ), which in some cases may be small compared to systematics. The uncertainties on the mass determinations should therefore be considered as lower limits, to which some systematics could be added. As a result, the cumulative distribution of the relative precision presented in Fig. 3 is optimistic and gives an upper limit to the amount of accurate estimates. Therefore, even with mass estimates available for more than 250 small bodies, our knowledge is still very limited: Only about half of the estimates are more accurate than 20%, and no more than 70% of the estimates are more accurate than 50% (higher uncertainties preventing any firm conclusion).

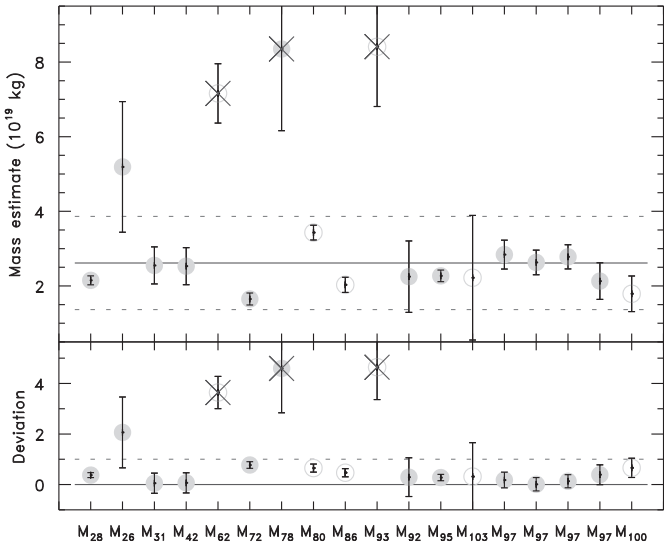

Fig. 2. The 18 mass estimates for (52) Europa (see Appendix D for the references). **Top:** The different mass estimates M_i, in 10^{19} kg. Symbols indicate the method used to determine the mass: deflections (gray disk) or planetary ephemeris (open circle). Crossed estimates were discarded from the analysis (see text). Horizontal solid and dashed lines are respectively the weighted average (μ) and standard deviation (σ) of the mass estimates before selection. **Bottom:** Same as above, but plotted as a function of the distance to the average value, in units of deviation: $(M_i-\mu)/\sigma$. Similar plots for each of the 140 small bodies with multiple mass estimates are provided in Appendix A.

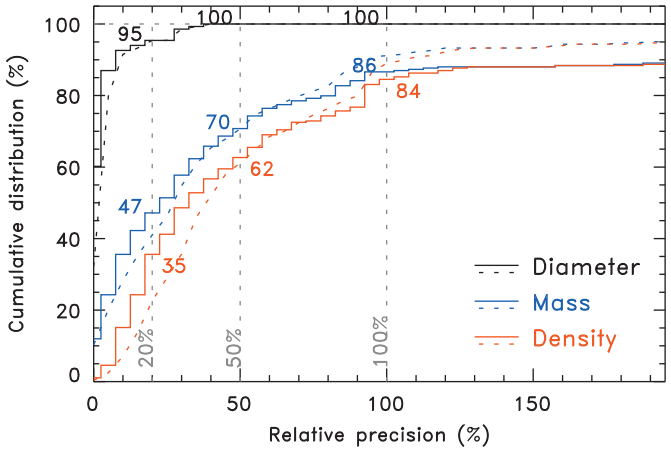

Fig. 3. Cumulative distribution of the accuracy on the diameter (black), mass (blue), and density (red) estimates. Dashed and solid lines represent the distributions before and after selection of best estimates (see text for details). Three reference levels for the relative accuracy are drawn: 20%, 50% and 100%, with the fraction of targets with a better accuracy reported for each estimate (after selection only). (For interpretation of the references to color in this figure caption, the reader is referred to the web version of this article.)

4.2. Volume estimates

As already noted by several authors, the most problematic part of determining the density of a small body is to measure any mass at all (*e.g.*, Merline et al., 2002; Consolmagno et al., 2008). The number of density estimates presented here is limited by the number of mass estimates, and not by the number of volume estimates (generally reported as volume-equivalent diameter, hereafter ϕ). Many different observing techniques and methods of analysis have been used to evaluate the diameter of small bodies (see the review by Carry et al., 2012). The 1454 diameter estimates listed in Appendix B were derived with 15 different methods, that can be grouped into four categories:

1. *Absolute magnitude*: It could almost be considered an *absence* of size estimate. It is the crudest method to evaluate the diameter of a small body (Fig. 4a). From the absolute magnitude H and an *assumed* geometric albedo p, the diameter is given by $\phi(\mathrm{km}) = 1329p^{-0.5}10^{-0.2H}$ (Pravec and Harris, 2007, and references therein). The diameter of 29 small bodies presented here were derived using their absolute magnitude, in the absence of any other estimates. This particularly applies to TNOs.
2. *Thermal modeling of mid-infrared radiometry*: It is by far the main provider of diameter estimates: 1233 diameter estimates out of the 1454 listed in Appendix B (*i.e.*, $\approx 85\%$). Asteroids are indeed among the brightest sources in the sky at mid-infrared wavelengths ($5-20\,\mu$m), so infrared satellites (IRAS, ISO, AKARI, Spitzer, and WISE) have been able to acquire observations of a vast number of these objects (see, Tedesco et al., 2002; Ryan and Woodward, 2010; Usui et al., 2011; Masiero et al., 2011; Mueller et al., 2011). The diameter and albedo of the colder TNOs have also been studied at longer wavelengths with Spitzer and Herschel (*e.g.*, Stansberry et al., 2008; Müller et al., 2009). As visible in Fig. 4b, the typical uncertainty is of only few percent. In many case, however, the different estimates from thermal modeling disagree above their respective quoted uncertainty (see Table 3 in Delbo and Tanga (2009), illustrating the issue). For instance, in the case of Europa (Fig. 5), both diameter estimates ϕ_{64} (Ryan and Woodward, 2010) were based on the same data, but used two different thermal modeling, and disagree at more than 6σ. Such differences are again indicative of underestimated uncertainties. Accuracy is often reported as the formal standard deviation (σ), which in some cases may be small compared to systematics. In the present case, the simplified standard thermal model (Lebofsky et al., 1986) and near-Earth asteroid thermal model (Harris, 1998) widely used do not take into account the spin and shape of the small body into account, and can therefore be strongly biased. A more realistic level of accuracy is about 10% (Lim et al., 2010), at which these estimates are still highly valuable given the huge number of small bodies that have been studied that way.
3. *Direct measurements of a single geometry*: Stellar occultations or disk-resolved images can provide an extremely precise measure of the apparent size and shape of a small body (*e.g.*, Brown and Trujillo, 2004; Brown et al., 2006; Marchis et al., 2006, 2008a; Dunham et al., 2011). When these direct measurements are limited to a single geometry, however, the evaluation of the diameter may be biased. The volume is 3-D while a single geometry only provides 2-D constraints. The typical accuracy of 5% (Fig. 4c) may therefore be optimistic. Nevertheless, these estimates are highly valuable, being based on direct measurements.
4. *Shape modeling based on several geometries:* The least numerous but most precise diameter estimates are derived when the spin and 3-D shape of the objects are modeled, thus limiting the 2-D to 3-D related biases (Fig. 4d). Small bodies can be modeled as smooth tri-axial ellipsoids (*e.g.*, Thomas et al., 2005; Schmidt et al., 2009; Drummond et al., 2009, 2010), convex shapes (Descamps et al., 2007; Ďurech et al., 2011), or realistic 3-D shapes (Veverka et al., 2000; Ostro et al., 2006, 2010; Carry et al., 2010a, 2010b; Sierks et al., 2011). In particular, spacecraft encounters with (25 143) Itokawa and (21) Lutetia have shown that multi-data approaches provide

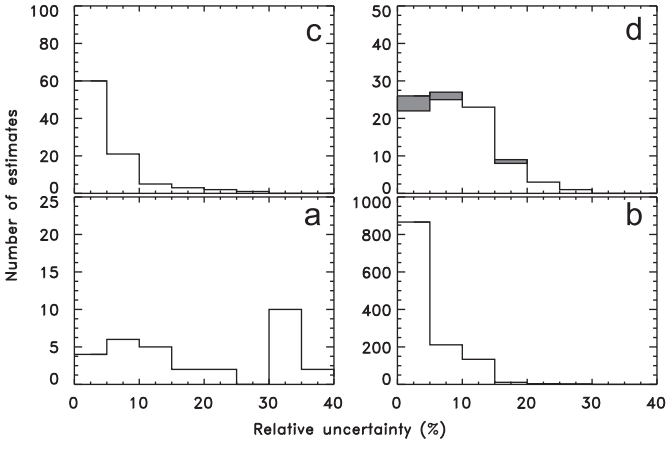

Fig. 4. Distribution of the relative accuracy of diameter estimates obtained with four classes of different methods (see text): (a) crude estimates from absolute magnitude, (b) thermal radiometry, (c) direct measurement limited to a single geometry, and (d) shape modeling based on several geometries (gray bars represent the diameters derived from spacecraft encounters). Although estimates in sub-plot (d) are expected to be the most precise, it is not reflected in their relative uncertainty distribution. The possible underestimation of biases in other techniques may be the cause (see text).

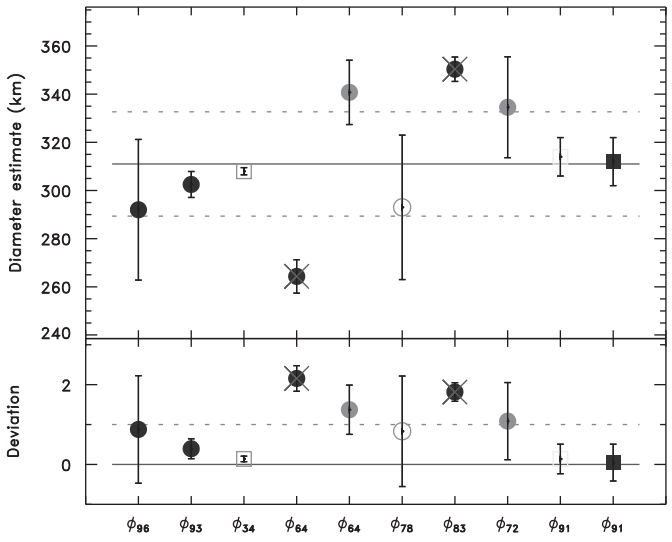

Fig. 5. The 10 diameter estimates for (52) Europa (see Appendix D for the references). **Top:** The different diameter estimates ϕ_i, in km. Symbols indicate the method used to determine the diameter: mid-infrared radiometry modeled using the Standard Thermal Model (STM: ϕ_{96}, ϕ_{93}, ϕ_{64}, and ϕ_{83}) and the near-Earth asteroid thermal model (NEATM: ϕ_{64} and ϕ_{72}), disk-resolved imaging on a single epoch (ϕ_{34}), combination of lightcurves and stellar occultations (ϕ_{78}), or shape modeling (ϕ_{91}). See Appendix B for a complete description of the symbols. Crossed estimates were discarded from the analysis (see text). Horizontal solid and dashed lines are respectively the weighted average (μ) and standard deviation (σ) of the diameter estimates before selection. **Bottom:** Same as above, but plotted as a function of the distance to the average value, in units of deviation: $(\phi_i - \mu)/\sigma$. Similar plots for each of the 258 small bodies with multiple diameter estimates are provided in Appendix B.

reliable and precise diameter estimates: *e.g.*, lightcurve-derived shape model with thermal radiometry (Mueller et al., 2006) or combined inversion of disk-resolved imaging and lightcurves (Kaasalainen, 2011; Carry et al., 2010b, 2012).

As visible in Figs. 3 and 4, the diameter estimates are generally intrinsically much more precise than the mass determination: all the estimates are known to better than 50% relative precision, and a large majority to better than 10%. Diameter estimates from different techniques moreover generally agree, suggesting that systematics are commensurable with formal uncertainties. The same selection criteria than for mass estimates were applied here, and about 15% of the estimates were discarded. Paradoxically, once the mass is determined, the uncertainty on the volume ($\delta V/V$) often becomes the major source of uncertainty on the density (ρ). Indeed,

$$\frac{\delta\rho}{\rho}=\sqrt{\left(\frac{\delta M}{M}\right)^2+\left(\frac{\delta V}{V}\right)^2}=\sqrt{\left(\frac{\delta M}{M}\right)^2+9\left(\frac{\delta\phi}{\phi}\right)^2} \quad (1)$$

The contribution of the uncertainty on the diameter ($\delta\phi/\phi$) therefore easily overwhelms that of the mass ($\delta M/M$) . In the compilation presented here, however, the mass is the limiting factor for 61% of the objects, contributing to $\approx$ 72% of the density uncertainty. This is mainly due to the high number of non-precise mass estimates (Fig. 3). If only the density estimates with a relative precision better than 20% are considered, then the situation is reversed: the diameter is the limiting factor for 75% of the objects, contributing to $\approx$68% of the density uncertainty. For these reasons, the mass should therefore be considered the limiting factor in most of the cases. As already discussed elsewhere, however, when a reliable mass estimate is available (*i.e.*, usually from the presence of a satellite), the precision on the volume generally limits the accuracy on the density (Merline et al., 2002; Britt et al., 2002; Consolmagno et al., 2008).

4.3. Indirect density estimates

For small bodies with diameters of a few to tens of kilometers the methods to estimate their mass listed above (Section 4.1) cannot be used. The gravitational influence of these very small bodies is too tiny to be measured. Even in the case of binary systems, their angular extent is generally too small to be imaged with current technology. The only exception are the small binary NEAs that can be imaged with radar during close approaches with Earth. Yet, a large fraction of the currently known binaries are small-sized systems discovered by studying their lightcurves (86 out of 207, *e.g.*, Mottola and Lahulla (2000); Pravec et al. (2002, 2006)). Indeed, photometric observations of the mutual eclipses of a system provide many constraints, for instance, on the ratio between the diameters of the two components or between the primary diameter and the orbit semi-major axis (see, Scheirich and Pravec, 2009).

Nevertheless, these parameters are dimensionless from lightcurve observations only. The *absolute* scale, hence semi-major axis and thus mass, cannot be derived. Usually, both components are *assumed* to have the same bulk density to bypass this restriction (*e.g.*, Scheirich and Pravec, 2009). These estimates are indirect, being derived without measuring the mass nor the size. The accuracy reached greatly depends on each system, and ranges from a few percent to 100% (Fig. 1d). It is worth noting that if small-sized binaries are formed by rotational breakup (Walsh et al., 2008) as suggested by the fast rotations of the primaries (Pravec et al., 2002, 2006, 2010), the porosity, hence density, of the components may be significantly different. These density estimates may therefore be biased, in the absence of an independent measure of the scale of the systems.

Measuring the mass of comets is another challenge. With diameters typically smaller than 10 km, comets have very small masses. In the absence of a satellite, studying their gravitational effect on other objects is hopeless. The activity of their nucleus however provides an indirect way to estimate their mass. Indeed, the forces resulting from the gas jets slowly change the orbit of the nucleus around the Sun. Modeling this non-gravitational effect provides the mass of the nucleus (*e.g.*, Davidsson and Gutiérrez, 2004, 2005, 2006; Davidsson et al., 2007; Sosa and Fernández, 2009). The masses of 11 comets have been derived using this approach. Richardson et al. (2007) have also studied the expansion of ejecta created by the Deep Impact experiment on the comet 9P/Tempel1. This is the most direct measurement of the mass of a comet, independent of the non-gravitational effect.

A summary of the mass, volume-equivalent diameter and bulk density of the 287 small bodies compiled here is provided in Table 1. The values listed are the weighted average and standard deviation of all the selected estimates (see Appendixes A–C). The density is given normalized to that of liquid water (1000 kg m^{-3}), *i.e.*, dimensionless. The estimates have been ranked from A to E, owing to the level of relative accuracy achieved on the density: B better than 20%, C between 20 and 50%, D between 50 and 100%, and E cruder than 100%. A stands for reliable estimates (more precise than 20%), based on more than five mass estimates and five diameter estimates, or a spacecraft encounter. Irrelevant densities are tagged with a cross (✗). Only about a third of the 287 density estimates have a relative precision better than 20% (Fig. 3), and two third better than 50%, above which level nothing relevant can be derived.

The fraction of volume occupied by voids, the macroporosity $\mathcal{P}$, is also reported, computed as:

$$\mathcal{P}(\%)=100\left(1-\frac{\rho}{\rho_m}\right) \quad (2)$$

with ρ the asteroid bulk density and ρ_m the bulk density of the associated meteorite (Table 2). The macroporosity is the least constrained of all the quantities discussed here. Indeed, it is affected by the uncertainties and possible biases on the diameter and mass estimates and also from the possible ambiguous links with meteorites (Section 2 and Table 3). Depending on the meteorite association, the macroporosity may change by 30–40%. For instance, while (16) Psyche was the most porous asteroid listed by Britt et al. (2002) and Consolmagno et al. (2008) with a macroporosity of about 70%, it stands in the low macroporosity range (about 18%). A low macroporosity is actually more consistent with the link between Psyche and iron meteorites than the very high value of $\sim$75% found previously.

5. Density and macroporosity of small bodies

The density and macroporosity of small bodies and their relationships with asteroid taxonomy, dynamical class, and diameter are discussed here.

For asteroids, the distribution of density estimates over taxonomic classes is presented in Fig. 6. The taxonomy is based on a limited sample (371 objects, see, DeMeo et al., 2009) and the relative part represented by each class in the whole population may be substantially different (Bus, 1999) but this discussion is beyond the scope of present analysis. Density estimates are available for the three complexes: 109 for C-complex, and 50 for both S- and X-complexes. End-members are less represented: only 15 density estimates are available, although end-members represent about 20% of the asteroids. For density estimates with

Table 1
Compilation of the average mass (M) and volume-equivalent diameter (ϕ) estimates (see Appendixes A–C), and resulting bulk density (ρ) and macroporosity ($\mathcal{P}$) for 287 objects, with their associated uncertainties. For each object, the dynamical class is listed (Dyn.), together with the taxonomic class (Tax., for asteroids only) and associated meteorite (Met.). The density estimates are ranked A–E, owing to the level of confidence at which they are determined (see text). Unrealistic density estimates are marked with a cross (✗) and uncertainties on the macroporosity larger than 100% are listed as ∞. **References**: (1) Clark et al. (2010), (2) Ockert-Bell et al. (2010), and (3) Fornasier et al. (2011). An electronic version of this table is available at https://genoide.imcce.fr/tools/public/densities.php.

Designation		Classification			Masses (kg)			Diameter (km)			Density		Porosity		Rank
#	Name	Dyn.	Tax.	Met.	M	δM	Fig.	ϕ	$\delta\phi$	Fig.	ρ	$\delta\rho$	$\mathcal{P}$	$\delta\mathcal{P}$	
1	Ceres	MBA	C	CM	9.44	$\pm 0.06\times10^{20}$	A.1	944.79	±22.99	B.1	2.13	±0.15	4	±1	A
2	Pallas	MBA	B	CK[1]	2.04	$\pm 0.04\times10^{20}$	A.2	514.41	±19.12	B.2	2.86	±0.32	0	±11	A
3	Juno	MBA	Sq	OC	2.73	$\pm 0.29\times10^{19}$	A.3	241.79	±10.58	B.3	3.68	±0.62	0	±16	A
4	Vesta	MBA	V	HED	2.63	$\pm 0.05\times10^{20}$	A.4	519.33	±6.84	B.4	3.58	±0.15	0	±4	A
5	Astraea	MBA	S	OC	2.64	$\pm 0.44\times10^{18}$	A.5	113.41	±3.53	B.5	3.45	±0.66	0	±19	B
6	Hebe	MBA	S	OC	1.39	$\pm 0.10\times10^{19}$	A.6	190.92	±7.15	B.6	3.81	±0.50	0	±13	A
7	Iris	MBA	S	OC	1.29	$\pm 0.21\times10^{19}$	A.7	225.89	±25.94	B.7	2.14	±0.81	35	±38	C
8	Flora	MBA	S	OC	9.17	$\pm 1.75\times10^{18}$	A.8	139.12	±2.26	B.8	6.50	±1.28	0	±19	✗
9	Metis	MBA	S	OC	8.39	$\pm 1.67\times10^{18}$	A.9	164.46	±7.67	B.9	3.60	±0.87	0	±24	C
10	Hygiea	MBA	C	CM	8.63	$\pm 0.52\times10^{19}$	A.10	421.60	±25.69	B.10	2.19	±0.42	2	±19	A
11	Parthenope	MBA	Sq	OC	5.91	$\pm 0.45\times10^{18}$	A.11	151.07	±5.11	B.11	3.27	±0.41	1	±12	A
12	Victoria	MBA	L	CO	2.45	$\pm 0.46\times10^{18}$	A.12	124.09	±8.31	B.12	2.45	±0.67	19	±27	C
13	Egeria	MBA	Ch	CM	8.82	$\pm 4.25\times10^{18}$	A.13	214.73	±11.53	B.13	1.70	±0.86	24	±50	D
14	Irene	MBA	S	OC	2.91	$\pm 1.88\times10^{18}$	A.14	147.75	±5.03	B.14	1.72	±1.12	48	±65	D
15	Eunomia	MBA	K	CV	3.14	$\pm 0.18\times10^{19}$	A.15	256.63	±1.04	B.15	3.54	±0.20	0	±5	B
16	Psyche	MBA	Xk	Ata[2]	2.72	$\pm 0.75\times10^{19}$	A.16	248.45	±17.13	B.16	3.38	±1.16	15	±34	C
17	Thetis	MBA	S	OC	1.33	$\pm 0.12\times10^{18}$	A.17	82.76	±8.79	B.17	4.48	±1.48	0	±33	C
18	Melpomene	MBA	S	OC	3.22	$\pm 1.28\times10^{18}$	A.18	141.72	±4.86	B.18	2.15	±0.88	35	±41	C
19	Fortuna	MBA	Ch	CM	8.60	$\pm 1.46\times10^{18}$	A.19	206.90	±6.49	B.19	1.85	±0.35	17	±19	A
20	Massalia	MBA	S	OC	5.00	$\pm 1.04\times10^{18}$	A.20	136.99	±8.82	B.20	3.71	±1.05	0	±28	C
21	Lutetia	MBA	Xk	EH[2]	1.70	$\pm 0.01\times10^{18}$	A.21	98.00	±5.00	B.21	3.44	±0.52	0	±15	A
22	Kalliope	MBA	X	Ata[2]	7.96	$\pm 0.31\times10^{18}$	A.22	170.23	±10.46	B.22	3.08	±0.58	23	±18	B
23	Thalia	MBA	S	OC	1.96	$\pm 0.09\times10^{18}$	A.23	106.81	±3.23	B.23	3.07	±0.31	7	±10	B
24	Themis	MBA	C	CM[1]	5.89	$\pm 1.91\times10^{18}$	A.24	183.84	±11.40	B.24	1.81	±0.67	19	±37	C
25	Phocaea	MBA	S	OC	5.99	$\pm 0.60\times10^{17}$	A.25	80.19	±4.66	B.25	2.21	±0.44	33	±20	C
26	Proserpina	MBA	S	OC	7.48	$\pm 8.95\times10^{17}$		89.63	±3.55	B.26	1.98	±2.38	40	$\pm\infty$	E
27	Euterpe	MBA	S	OC	1.67	$\pm 1.01\times10^{18}$	A.26	105.80	±7.23	B.27	2.69	±1.71	19	±63	D
28	Bellona	MBA	S	OC	2.62	$\pm 0.15\times10^{18}$	A.27	108.10	±11.49	B.28	3.95	±1.28	0	±32	C
29	Amphitrite	MBA	S	OC	1.29	$\pm 0.20\times10^{19}$	A.28	217.59	±10.71	B.29	2.38	±0.51	28	±21	C
30	Urania	MBA	S	OC	1.74	$\pm 0.49\times10^{18}$	A.29	94.48	±5.37	B.30	3.92	±1.29	0	±32	C
31	Euphrosyne	MBA	C	CM	1.27	$\pm 0.65\times10^{19}$	A.30	272.92	±8.85	B.31	1.18	±0.61	47	±52	D
33	Polyhymnia	MBA	S	OC	6.20	$\pm 0.74\times10^{18}$		53.98	±0.91		75.28	±9.71	0	±12	✗
34	Circe	MBA	Ch	CM	3.66	$\pm 0.03\times10^{18}$	A.31	113.02	±4.90	B.32	4.83	±0.63	0	±13	✗
36	Atalante	MBA	C	CM	4.32	$\pm 3.80\times10^{18}$		110.14	±4.38	B.33	6.17	±5.48	0	±88	E
38	Leda	MBA	Cgh	CM	5.71	$\pm 5.47\times10^{18}$		115.41	±1.33	B.34	7.09	±6.79	0	±95	E
39	Laetitia	MBA	S	OC	4.72	$\pm 1.14\times10^{18}$	A.32	153.80	±4.14	B.35	2.47	±0.63	25	±25	C
41	Daphne	MBA	Ch	CM	6.31	$\pm 0.11\times10^{18}$	A.33	181.05	±9.60	B.36	2.03	±0.32	9	±16	B
42	Isis	MBA	S	OC	1.58	$\pm 0.52\times10^{18}$	A.34	102.73	±2.73	B.37	2.78	±0.93	16	±33	C
43	Ariadne	MBA	Sq	OC	1.21	$\pm 0.22\times10^{18}$	A.35	63.61	±4.66	B.38	8.99	±2.57	0	±28	✗
45	Eugenia	MBA	C	CM	5.79	$\pm 0.14\times10^{18}$	A.36	201.81	±14.77	B.39	1.34	±0.29	40	±22	C
46	Hestia	MBA	Xc	Mes	5.99	$\pm 0.49\times10^{18}$	A.37	125.29	±5.21	B.40	5.81	±0.87	0	±14	E
47	Aglaja	MBA	B	CV	3.25	$\pm 1.68\times10^{18}$	A.38	141.90	±8.72	B.41	2.17	±1.19	22	±55	D
48	Doris	MBA	Ch	CM	6.12	$\pm 2.96\times10^{18}$	A.39	211.67	±10.85	B.42	1.23	±0.62	45	±50	D
49	Pales	MBA	Ch	CM	4.22	$\pm 2.15\times10^{18}$	A.40	150.82	±3.81	B.43	2.35	±1.21	0	±51	D
50	Virginia	MBA	Ch	CM[3]	2.31	$\pm 0.70\times10^{18}$	A.41	99.42	±0.46	B.44	4.49	±1.35	0	±30	E
51	Nemausa	MBA	Ch	CM	2.48	$\pm 0.86\times10^{18}$	A.42	148.85	±3.56	B.45	1.43	±0.50	36	±35	C
52	Europa	MBA	C	CM	2.38	$\pm 0.58\times10^{19}$	A.43	310.21	±10.34	B.46	1.52	±0.39	32	±26	C
53	Kalypso	MBA	C	CM	5.63	$\pm 5.00\times10^{18}$		109.06	±7.27	B.47	8.28	±7.54	0	±91	✗
54	Alexandra	MBA	Cgh	CM	6.16	$\pm 3.50\times10^{18}$	A.44	149.68	±9.85	B.48	3.50	±2.11	0	±60	D
56	Melete	MBA	Xk	Mes	4.61	$\pm 0.00\times10^{18}$	A.45	113.63	±8.27	B.49	6.00	±1.31	0	±21	C

57	Mnemosyne	MBA	S	OC	1.26	$\pm 0.24\times10^{19}$	A.46	113.01	±4.46	B.50	16.62	±3.73	0	±22	✗
59	Elpis	MBA	B	CV	3.00	$\pm 0.50\times10^{18}$	A.47	163.61	±6.50	B.51	1.30	±0.26	53	±20	C
60	Echo	MBA	S	Ec	3.15	$\pm 0.32\times10^{17}$	A.48	60.00	±1.33	B.52	2.78	±0.33	16	±12	B
61	Danae	MBA	S	OC	2.89	$\pm 2.78\times10^{18}$		82.52	±2.73	B.53	9.81	±9.49	0	±96	D
63	Ausonia	MBA	S	OC	1.53	$\pm 0.15\times10^{18}$	A.49	94.45	±7.15	B.54	3.46	±0.86	0	±24	C
65	Cybele	MBA	Xk	Mes	1.36	$\pm 0.31\times10^{19}$	A.50	248.29	±17.59	B.55	1.70	±0.52	59	±30	C
67	Asia	MBA	S	OC	1.03	$\pm 0.10\times10^{18}$		60.99	±2.41	B.56	8.66	±1.32	0	±15	✗
68	Leto	MBA	S	OC	3.28	$\pm 1.90\times10^{18}$	A.51	124.96	±6.42	B.57	3.21	±1.92	3	±60	D
69	Hesperia	MBA	Xk	Mes	5.86	$\pm 1.18\times10^{18}$	A.52	136.69	±4.71	B.58	4.38	±0.99	0	±22	C
70	Panopaea	MBA	Cgh	CM	4.33	$\pm 1.09\times10^{18}$		133.43	±7.58	B.59	3.48	±1.05	0	±30	C
72	Feronia	MBA	D	CM	3.32	$\pm 8.49\times10^{18}$		83.95	±4.02	B.60	10.71	±27.44	0	±∞	✗
74	Galatea	MBA	C	CM	6.13	$\pm 5.36\times10^{18}$		120.67	±7.15	B.61	6.66	±5.94	0	±89	D
76	Freia	MBA	C	CM	1.97	$\pm 4.20\times10^{18}$	A.53	167.87	±8.73	B.62	0.79	±1.69	64	±CO	E
77	Frigga	MBA	Xe	EH[2]	1.74	$\pm 0.68\times10^{18}$		66.97	±1.28	B.63	11.05	±4.34	0	±39	✗
78	Diana	MBA	Ch	CM	1.27	$\pm 0.13\times10^{18}$	A.54	123.63	±4.57	B.64	1.28	±0.19	42	±14	B
81	Terpsichore	MBA	Cb	CM	6.19	$\pm 5.31\times10^{18}$		121.77	±2.34	B.65	6.54	±5.62	0	±85	D
84	Klio	MBA	Ch	CM	5.47	$\pm 4.06\times10^{17}$		79.40	±1.95	B.66	2.08	±1.55	7	±74	D
85	Io	MBA	Cb	CM	2.57	$\pm 1.48\times10^{18}$	A.55	155.00	±6.00	B.67	1.31	±0.77	41	±58	D
87	Sylvia	MBA	X	CV	1.48	$\pm 0.00\times10^{19}$	A.56	278.14	±10.75	B.68	1.31	±0.15	52	±11	B
88	Thisbe	MBA	B	CV	1.53	$\pm 0.31\times10^{19}$	A.57	204.04	±9.12	B.69	3.44	±0.84	0	±24	C
89	Julia	MBA	X	CV	6.71	$\pm 1.82\times10^{18}$	A.58	147.57	±8.32	B.70	3.98	±1.27	0	±31	C
90	Antiope	MBA	C	CM	8.30	$\pm 0.20\times10^{17}$	A.59	122.15	±2.77	B.71	0.86	±0.06	61	±7	B
92	Undina	MBA	Xk	Mes	4.43	$\pm 0.25\times10^{18}$	A.60	124.44	±3.25	B.72	4.39	±0.42	0	±9	B
93	Minerva	MBA	C	CM	3.50	$\pm 0.40\times10^{18}$		149.79	±8.08	B.73	1.98	±0.39	11	±19	B
94	Aurora	MBA	C	CM	6.23	$\pm 3.64\times10^{18}$	A.61	186.35	±8.84	B.74	1.83	±1.10	18	±60	D
96	Aegle	MBA	T	Ata	6.48	$\pm 6.26\times10^{18}$	A.62	167.92	±5.49	B.75	2.61	±2.53	34	±97	D
97	Klotho	MBA	Xc	Ata[2]	1.33	$\pm 0.13\times10^{18}$		84.79	±3.13	B.76	4.16	±0.62	0	±14	B
98	Ianthe	MBA	Ch	CM	8.93	$\pm 1.99\times10^{17}$	A.63	106.16	±3.76	B.77	1.42	±0.35	36	±24	C
105	Artemis	MBA	Ch	CM	1.53	$\pm 0.54\times10^{18}$	A.64	119.10	±6.78	B.78	1.73	±0.67	23	±38	C
106	Dione	MBA	Cgh	CM	3.06	$\pm 1.54\times10^{18}$	A.65	147.17	±3.34	B.79	1.83	±0.92	18	±50	D
107	Camilla	MBA	X	CV	1.12	$\pm 0.03\times10^{19}$	A.66	210.68	±8.89	B.80	2.28	±0.29	18	±12	B
111	Ate	MBA	Ch	CM	1.76	$\pm 0.44\times10^{18}$	A.67	142.85	±5.94	B.81	1.15	±0.32	48	±27	C
112	Iphigenia	MBA	Ch	CM	1.97	$\pm 6.78\times10^{18}$		71.07	±0.52	B.82	10.48	±36.06	0	±∞	✗
117	Lomia	MBA	X	CV	6.08	$\pm 0.63\times10^{18}$	A.68	146.78	±3.96	B.83	3.67	±0.48	0	±13	B
121	Hermione	MBA	Ch	CM	4.97	$\pm 0.33\times10^{18}$	A.69	195.36	±10.62	B.84	1.27	±0.22	43	±17	B
126	Velleda	MBA	S	OC	0.47	$\pm 5.79\times10^{18}$		44.79	±1.33	B.85	10.00	±123.00	0	±∞	✗
127	Johanna	MBA	Ch	CM	3.08	$\pm 1.35\times10^{18}$	A.70	116.14	±3.93	B.86	3.75	±1.68	0	±44	C
128	Nemesis	MBA	C	CM	5.97	$\pm 2.56\times10^{18}$	A.71	184.19	±5.19	B.87	1.82	±0.79	18	±43	C
129	Antigone	MBA	X	Ste[2]	2.65	$\pm 0.89\times10^{18}$	A.72	119.44	±3.91	B.88	2.96	±1.04	29	±35	C
130	Elektra	MBA	Ch	CM	6.60	$\pm 0.40\times10^{18}$	A.73	189.62	±6.81	B.89	1.84	±0.22	17	±12	B
132	Aethra	MBA	Xe	EH	0.41	$\pm 2.71\times10^{18}$		35.83	±6.59	B.90	17.09	±112.83	0	±∞	✗
135	Hertha	MBA	Xk	Ata[2]	1.21	$\pm 0.16\times10^{18}$	A.74	76.12	±3.29	B.91	5.23	±0.96	0	±18	B
137	Meliboea	MBA	C	CM	7.27	$\pm 3.07\times10^{18}$	A.75	145.92	±3.58	B.92	4.46	±1.91	0	±42	E
138	Tolosa	MBA	S	OC	4.93	$\pm 2.59\times10^{17}$		51.86	±3.07	B.93	6.74	±3.74	0	±55	E
139	Juewa	MBA	X	CV	5.54	$\pm 2.20\times10^{18}$	A.76	161.43	±7.38	B.94	2.51	±1.05	9	±41	C
141	Lumen	MBA	Ch	CM	8.25	$\pm 5.77\times10^{18}$		131.35	±5.21	B.95	6.95	±4.93	0	±70	✗
144	Vibilia	MBA	Ch	CM	5.30	$\pm 1.20\times10^{18}$	A.77	141.34	±2.76	B.96	3.58	±0.84	0	±23	C
145	Adeona	MBA	Ch	CM	2.08	$\pm 0.57\times10^{18}$	A.78	149.50	±5.45	B.97	1.18	±0.34	47	±29	C
147	Protogeneia	MBA	C	CM	1.23	$\pm 0.05\times10^{19}$		118.44	±10.45	B.98	14.13	±3.78	0	±26	✗
148	Gallia	MBA	S	OC	4.89	$\pm 1.67\times10^{18}$		83.45	±5.07	B.99	16.06	±6.22	0	±38	✗
150	Nuwa	MBA	C	CM	1.62	$\pm 0.20\times10^{18}$	A.79	146.54	±9.15	B.100	0.98	±0.22	56	±22	C
152	Atala	MBA	S	OC	5.43	$\pm 1.24\times10^{18}$		60.03	±3.01	B.101	47.92	±13.10	0	±27	✗
154	Bertha	MBA	Cb	CM	9.19	$\pm 5.20\times10^{18}$	A.80	186.85	±1.83	B.102	2.69	±1.52	0	±56	D
156	Xanthippe	MBA	Ch	CM	6.49	$\pm 3.71\times10^{18}$		116.34	±4.14	B.103	7.86	±4.57	0	±58	✗
163	Erigone	MBA	Ch	CM	2.01	$\pm 0.68\times10^{18}$		72.70	±1.95	B.104	9.99	±3.45	0	±34	✗
164	Eva	MBA	X	Ev	9.29	$\pm 7.76\times10^{17}$		101.77	±3.61	B.105	1.68	±1.41	39	±84	D
165	Loreley	MBA	C	CM	1.91	$\pm 0.19\times10^{19}$	A.81	164.92	±8.14	B.106	8.14	±1.46	0	±17	✗
168	Sibylla	MBA	Ch	CM	3.92	$\pm 1.80\times10^{18}$	A.82	149.06	±4.29	B.107	2.26	±1.05	0	±46	C
173	Ino	MBA	X	CV	4.79	$\pm 3.11\times10^{18}$	A.83	160.07	±6.04	B.108	2.23	±1.47	20	±65	D
179	Klytaemnestra	MBA	S	OC	2.49	$\pm 1.19\times10^{17}$		75.02	±3.21	B.109	1.12	±0.55	66	±49	C

Table 1 (*continued*)

Designation		Classification			Masses (kg)			Diameter (km)			Density		Porosity		Rank
#	Name	Dyn.	Tax.	Met.	M	δM	Fig.	ϕ	$\delta\phi$	Fig.	ρ	$\delta\rho$	$\mathcal{P}$	$\delta\mathcal{P}$	
185	Eunike	MBA	C	CM	3.56	$\pm$ 2.61×10^{18}	A.84	160.61	$\pm$ 5.00	B.110	1.64	$\pm$ 1.21	27	$\pm$ 74	D
187	Lamberta	MBA	Ch	CM	1.80	$\pm$ 0.85×10^{18}	A.85	131.31	$\pm$ 1.08	B.111	1.51	$\pm$ 0.71	32	$\pm$ 47	C
189	Phthia	MBA	Sa	OC	3.84	$\pm$ 0.81×10^{16}		40.91	$\pm$ 1.36	B.112	1.07	$\pm$ 0.25	67	$\pm$ 23	C
192	Nausikaa	MBA	S	OC	1.79	$\pm$ 0.42×10^{18}	A.86	90.18	$\pm$ 2.80	B.113	4.64	$\pm$ 1.17	0	$\pm$ 25	C
194	Prokne	MBA	Ch	CM	2.68	$\pm$ 0.29×10^{18}	A.87	170.33	$\pm$ 6.92	B.114	1.03	$\pm$ 0.16	53	$\pm$ 16	B
196	Philomela	MBA	S	OC	4.00	$\pm$ 1.53×10^{18}	A.88	145.29	$\pm$ 7.71	B.115	2.48	$\pm$ 1.02	25	$\pm$ 41	C
200	Dynamene	MBA	Ch	CM	1.07	$\pm$ 0.16×10^{19}		130.71	$\pm$ 3.01	B.116	9.14	$\pm$ 1.51	0	$\pm$ 16	✗
204	Kallisto	MBA	S	OC	0.60	$\pm$ 1.81×10^{18}		50.36	$\pm$ 1.69	B.117	8.98	$\pm$ 27.07	0	$\pm\infty$	✗
209	Dido	MBA	Xc	Mes	4.59	$\pm$ 7.42×10^{18}		140.35	$\pm$ 10.12	B.118	3.17	$\pm$ 5.17	25	$\pm\infty$	E
210	Isabella	MBA	Cb	CM	3.41	$\pm$ 1.09×10^{18}		73.70	$\pm$ 8.47	B.119	16.26	$\pm$ 7.65	0	$\pm$ 47	✗
211	Isolda	MBA	Ch	CM	4.49	$\pm$ 2.43×10^{18}	A.89	149.81	$\pm$ 6.10	B.120	2.54	$\pm$ 1.41	0	$\pm$ 55	D
212	Medea	MBA	D	CM	1.32	$\pm$ 0.10×10^{19}		144.13	$\pm$ 7.23	B.121	8.41	$\pm$ 1.43	0	$\pm$ 17	✗
216	Kleopatra	MBA	Xe	Ata[2]	4.64	$\pm$ 0.20×10^{18}	A.90	127.47	$\pm$ 8.44	B.122	4.27	$\pm$ 0.86	0	$\pm$ 20	C
217	Eudora	MBA	X	CV	1.52	$\pm$ 0.06×10^{18}		68.62	$\pm$ 1.41	B.123	8.98	$\pm$ 0.65	0	$\pm$ 7	✗
221	Eos	MBA	K	CV	5.87	$\pm$ 0.34×10^{18}		103.52	$\pm$ 5.60	B.124	10.10	$\pm$ 1.74	0	$\pm$ 17	✗
230	Athamantis	MBA	S	OC	1.89	$\pm$ 0.19×10^{18}		110.17	$\pm$ 4.57	B.125	2.69	$\pm$ 0.43	19	$\pm$ 15	B
234	Barbara	MBA	L	CO	0.44	$\pm$ 1.45×10^{18}		45.62	$\pm$ 1.93	B.126	8.84	$\pm$ 29.17	0	$\pm\infty$	✗
238	Hypatia	MBA	Ch	CM	4.90	$\pm$ 1.70×10^{18}	A.91	146.13	$\pm$ 2.66	B.127	2.99	$\pm$ 1.05	0	$\pm$ 35	C
240	Vanadis	MBA	C	CM	1.10	$\pm$ 0.92×10^{18}	A.92	94.03	$\pm$ 5.37	B.128	2.53	$\pm$ 2.15	0	$\pm$ 84	D
241	Germania	MBA	Cb	CM	0.86	$\pm$ 5.00×10^{18}		178.60	$\pm$ 7.84	B.129	0.28	$\pm$ 1.67	87	$\pm\infty$	✗
243	Ida	MBA	S	OC	3.78	$\pm$ 0.20×10^{16}		31.29	$\pm$ 1.20	B.130	2.35	$\pm$ 0.29	29	$\pm$ 12	A
253	Mathilde	MBA	Cb	CM	1.03	$\pm$ 0.04×10^{17}	A.93	53.00	$\pm$ 2.59	B.131	1.32	$\pm$ 0.20	41	$\pm$ 15	A
259	Aletheia	MBA	X	CV	7.79	$\pm$ 0.43×10^{18}	A.94	190.05	$\pm$ 6.82	B.132	2.16	$\pm$ 0.26	22	$\pm$ 12	B
266	Aline	MBA	Ch	CM	4.15	$\pm$ 0.42×10^{18}		107.95	$\pm$ 6.62	B.133	6.29	$\pm$ 1.32	0	$\pm$ 20	E
268	Adorea	MBA	X	CV	3.25	$\pm$ 2.26×10^{18}	A.95	140.31	$\pm$ 3.34	B.134	2.24	$\pm$ 1.56	19	$\pm$ 69	D
283	Emma	MBA	C	CM[3]	1.38	$\pm$ 0.03×10^{18}	A.96	132.74	$\pm$ 10.13	B.135	1.12	$\pm$ 0.25	49	$\pm$ 23	C
304	Olga	MBA	Xc	Mes	1.15	$\pm$ 1.12×10^{18}		70.30	$\pm$ 2.32	B.136	6.31	$\pm$ 6.18	0	$\pm$ 97	D
306	Unitas	MBA	S	OC	5.33	$\pm$ 5.77×10^{17}		52.88	$\pm$ 3.48	B.137	6.88	$\pm$ 7.57	0	$\pm\infty$	E
322	Phaeo	MBA	D	CM	1.86	$\pm$ 0.04×10^{18}		71.88	$\pm$ 4.32	B.138	9.56	$\pm$ 1.73	0	$\pm$ 18	✗
324	Bamberga	MBA	Cb	CM	1.03	$\pm$ 0.10×10^{19}	A.97	234.67	$\pm$ 7.80	B.139	1.52	$\pm$ 0.20	32	$\pm$ 13	A
328	Gudrun	MBA	S	OC	3.16	$\pm$ 0.46×10^{18}	A.98	122.59	$\pm$ 3.72	B.140	3.27	$\pm$ 0.55	1	$\pm$ 17	B
334	Chicago	MBA	C	CM	5.06	$\pm$ 5.63×10^{18}	A.99	167.26	$\pm$ 7.27	B.141	2.06	$\pm$ 2.31	8	$\pm\infty$	E
337	Devosa	MBA	Xk	Hex3	1.08	$\pm$ 0.16×10^{18}	A.100	63.87	$\pm$ 3.14	B.142	7.91	$\pm$ 1.65	0	$\pm$ 20	✗
344	Desiderata	MBA	C	CM	1.39	$\pm$ 0.48×10^{18}	A.101	129.20	$\pm$ 3.37	B.143	1.22	$\pm$ 0.43	45	$\pm$ 35	C
345	Tercidina	MBA	Ch	CM	2.68	$\pm$ 1.18×10^{18}	A.102	98.78	$\pm$ 2.63	B.144	5.30	$\pm$ 2.37	0	$\pm$ 44	C
346	Hermentaria	MBA	S	OC	6.33	$\pm$ 0.18×10^{18}		93.27	$\pm$ 3.05	B.145	14.89	$\pm$ 1.52	0	$\pm$ 10	✗
349	Dembowska	MBA	R	OC	3.58	$\pm$ 1.03×10^{18}	A.103	145.23	$\pm$ 17.21	B.146	2.23	$\pm$ 1.01	33	$\pm$ 45	C
354	Eleonora	MBA	A	Pal	7.18	$\pm$ 2.57×10^{18}	A.104	154.34	$\pm$ 5.65	B.147	3.73	$\pm$ 1.39	21	$\pm$ 37	C
356	Liguria	MBA	Ch	CM	7.83	$\pm$ 1.50×10^{18}		134.76	$\pm$ 5.17	B.148	6.10	$\pm$ 1.36	0	$\pm$ 22	✗
365	Corduba	MBA	Ch	CM	5.84	$\pm$ 0.95×10^{18}		104.51	$\pm$ 2.42	B.149	9.76	$\pm$ 1.73	0	$\pm$ 17	✗
372	Palma	MBA	X	CV	5.15	$\pm$ 0.64×10^{18}	A.105	191.12	$\pm$ 2.68	B.150	1.40	$\pm$ 0.18	49	$\pm$ 13	B
375	Ursula	MBA	Xc	Mes	8.45	$\pm$ 5.26×10^{18}	A.106	191.65	$\pm$ 4.01	B.151	2.29	$\pm$ 1.43	46	$\pm$ 62	D
379	Huenna	MBA	C	CM[1]	3.83	$\pm$ 0.20×10^{17}		87.28	$\pm$ 5.70	B.152	1.10	$\pm$ 0.22	51	$\pm$ 20	C
381	Myrrha	MBA	X	CV	9.18	$\pm$ 0.80×10^{18}		123.41	$\pm$ 6.30	B.153	9.32	$\pm$ 1.64	0	$\pm$ 17	✗
386	Siegena	MBA	Ch	CM	8.14	$\pm$ 1.58×10^{18}	A.107	170.35	$\pm$ 8.40	B.154	3.14	$\pm$ 0.76	0	$\pm$ 24	C
387	Aquitania	MBA	L	CO	1.90	$\pm$ 0.64×10^{18}	A.108	103.51	$\pm$ 2.23	B.155	3.27	$\pm$ 1.11	0	$\pm$ 34	C
404	Arsinoe	MBA	B	CV	3.42	$\pm$ 3.03×10^{18}		96.97	$\pm$ 3.01	B.156	7.16	$\pm$ 6.38	0	$\pm$ 89	D
405	Thia	MBA	Ch	CM	1.38	$\pm$ 0.14×10^{18}		122.14	$\pm$ 7.69	B.157	1.44	$\pm$ 0.30	35	$\pm$ 21	C
409	Aspasia	MBA	Xc	Mes	1.18	$\pm$ 0.23×10^{19}	A.109	176.33	$\pm$ 4.50	B.158	4.10	$\pm$ 0.84	3	$\pm$ 20	C
410	Chloris	MBA	Ch	CM	6.24	$\pm$ 0.30×10^{18}	A.110	115.55	$\pm$ 8.22	B.159	7.72	$\pm$ 1.69	0	$\pm$ 21	✗
416	Vaticana	MBA	S	OC	3.27	$\pm$ 3.10×10^{18}		87.10	$\pm$ 2.57	B.160	9.44	$\pm$ 8.99	0	$\pm$ 95	D
419	Aurelia	MBA	Cb	CM[1]	1.72	$\pm$ 0.34×10^{18}	A.111	124.47	$\pm$ 3.08	B.161	1.70	$\pm$ 0.35	24	$\pm$ 21	C
420	Bertholda	MBA	X	CV	1.48	$\pm$ 0.09×10^{19}		141.54	$\pm$ 2.08	B.162	9.96	$\pm$ 0.75	0	$\pm$ 7	✗
423	Diotima	MBA	C	CM	6.91	$\pm$ 1.93×10^{18}	A.112	211.64	$\pm$ 16.02	B.163	1.39	$\pm$ 0.50	38	$\pm$ 35	C

433	Eros	NEA	S	OC	6.69	$\pm\ 0.00\times10^{15}$		16.85	$\pm$0.07	B.164	2.67	$\pm$0.03	1	$\pm$1	A
442	Eichsfeldia	MBA	Ch	CM	1.95	$\pm\ 0.20\times10^{17}$		65.58	$\pm$1.70	B.165	1.32	$\pm$0.16	41	$\pm$12	B
444	Gyptis	MBA	C	CM	1.06	$\pm\ 0.28\times10^{19}$	A.113	164.63	$\pm$2.60	B.166	4.55	$\pm$1.23	0	$\pm$27	C
445	Edna	MBA	Ch	CM	3.47	$\pm\ 0.78\times10^{18}$		88.60	$\pm$4.10	B.167	9.52	$\pm$2.50	0	$\pm$26	✗
449	Hamburga	MBA	C	CM	1.57	$\pm\ 1.40\times10^{18}$		66.76	$\pm$4.82	B.168	10.07	$\pm$9.24	0	$\pm$91	E
451	Patientia	MBA	Cb	CM	1.09	$\pm\ 0.53\times10^{19}$	A.114	234.42	$\pm$10.17	B.169	1.60	$\pm$0.80	28	$\pm$50	D
455	Bruchsalia	MBA	Xk	Mes	1.19	$\pm\ 0.12\times10^{18}$		88.13	$\pm$6.89	B.170	3.32	$\pm$0.84	21	$\pm$25	C
469	Argentina	MBA	Xk	Mes	4.53	$\pm\ 1.76\times10^{18}$	A.115	126.00	$\pm$4.91	B.171	4.32	$\pm$1.75	0	$\pm$40	C
471	Papagena	MBA	S	OC	3.05	$\pm\ 1.73\times10^{18}$	A.116	124.55	$\pm$8.77	B.172	3.01	$\pm$1.82	9	$\pm$60	D
481	Emita	MBA	Ch	CM	5.78	$\pm\ 1.45\times10^{18}$		107.23	$\pm$4.71	B.173	8.95	$\pm$2.53	0	$\pm$28	C
485	Genua	MBA	S	OC	1.36	$\pm\ 0.44\times10^{18}$		56.31	$\pm$4.15	B.174	14.53	$\pm$5.68	0	$\pm$39	✗
488	Kreusa	MBA	Ch	CM	2.48	$\pm\ 1.14\times10^{18}$	A.117	162.32	$\pm$9.54	B.175	1.10	$\pm$0.54	50	$\pm$49	C
490	Veritas	MBA	Ch	CM	5.99	$\pm\ 2.23\times10^{18}$	A.118	110.96	$\pm$3.80	B.176	8.37	$\pm$3.23	0	$\pm$38	C
491	Carina	MBA	X	CV	4.82	$\pm\ 1.95\times10^{18}$		97.36	$\pm$3.18	B.177	9.97	$\pm$4.15	0	$\pm$41	C
503	Evelyn	MBA	Ch	CM	2.85	$\pm\ 0.34\times10^{18}$		87.58	$\pm$3.58	B.178	8.10	$\pm$1.38	0	$\pm$17	✗
505	Cava	MBA	Xk	LL1	3.99	$\pm\ 3.84\times10^{18}$		101.51	$\pm$1.83	B.179	7.28	$\pm$7.02	0	$\pm$96	D
508	Princetonia	MBA	X	CV	2.99	$\pm\ 0.65\times10^{18}$	A.119	139.69	$\pm$3.40	B.180	2.09	$\pm$0.47	25	$\pm$22	C
511	Davida	MBA	C	CM	3.38	$\pm\ 1.02\times10^{19}$	A.120	298.28	$\pm$11.92	B.181	2.43	$\pm$0.79	0	$\pm$32	C
516	Amherstia	MBA	X	CV	1.43	$\pm\ 1.33\times10^{18}$		69.84	$\pm$4.38	B.182	8.01	$\pm$7.60	0	$\pm$94	D
532	Herculina	MBA	S	OC	1.15	$\pm\ 0.28\times10^{19}$	A.121	217.49	$\pm$5.10	B.183	2.12	$\pm$0.53	36	$\pm$25	C
536	Merapi	MBA	X	CV	2.61	$\pm\ 0.47\times10^{19}$	A.122	155.17	$\pm$3.53	B.184	13.36	$\pm$2.59	0	$\pm$19	✗
554	Peraga	MBA	Ch	CI1	6.59	$\pm\ 0.66\times10^{17}$	A.123	96.46	$\pm$1.68	B.185	1.40	$\pm$0.15	12	$\pm$11	B
582	Olympia	MBA	S	OC	0.43	$\pm\ 1.17\times10^{18}$		43.39	$\pm$1.49	B.186	10.00	$\pm$27.35	0	$\pm\infty$	✗
584	Semiramis	MBA	S	OC	8.23	$\pm\ 5.77\times10^{17}$		51.78	$\pm$2.15	B.187	11.31	$\pm$8.06	0	$\pm$71	✗
602	Marianna	MBA	Ch	CM	1.02	$\pm\ 0.05\times10^{19}$		127.95	$\pm$2.86	B.188	9.29	$\pm$0.76	0	$\pm$8	✗
604	Tekmessa	MBA	Xc	Mes	1.45	$\pm\ 0.28\times10^{18}$		64.42	$\pm$3.01	B.189	10.35	$\pm$2.46	0	$\pm$23	✗
617	Patroclus	MBA	X	CV	1.36	$\pm\ 0.11\times10^{18}$		143.14	$\pm$8.37	B.190	0.88	$\pm$0.17	68	$\pm$19	B
624	Hektor	MBA	X	CV	9.95	$\pm\ 0.12\times10^{18}$		226.68	$\pm$15.15	B.191	1.63	$\pm$0.32	41	$\pm$20	C
626	Notburga	MBA	Cb	CM	3.24	$\pm\ 1.30\times10^{18}$	A.124	96.84	$\pm$4.67	B.192	6.81	$\pm$2.90	0	$\pm$42	E
654	Zelinda	MBA	Ch	CM	1.35	$\pm\ 0.14\times10^{18}$		127.83	$\pm$5.23	B.193	1.23	$\pm$0.19	45	$\pm$15	B
665	Sabine	MBA	X	CV	6.98	$\pm\ 3.98\times10^{17}$		52.71	$\pm$0.72	B.194	9.10	$\pm$5.20	0	$\pm$57	E
675	Ludmilla	MBA	S	OC	1.20	$\pm\ 0.24\times10^{19}$		67.66	$\pm$0.94		73.99	$\pm$15.05	0	$\pm$20	✗
679	Pax	MBA	L	CO	7.14	$\pm\ 1.99\times10^{17}$		64.88	$\pm$3.64	B.195	4.99	$\pm$1.62	0	$\pm$32	C
680	Genoveva	MBA	X	CV	2.69	$\pm\ 0.04\times10^{18}$		84.69	$\pm$1.71	B.196	8.45	$\pm$0.52	0	$\pm$6	✗
690	Wratislavia	MBA	B	CV	1.28	$\pm\ 0.03\times10^{19}$		146.21	$\pm$11.02	B.197	7.81	$\pm$1.77	0	$\pm$22	✗
702	Alauda	MBA	B	CV	6.06	$\pm\ 3.60\times10^{18}$	A.125	191.65	$\pm$8.22	B.198	1.64	$\pm$0.99	41	$\pm$60	D
704	Interamnia	MBA	B	CI1	3.28	$\pm\ 0.45\times10^{19}$	A.126	317.19	$\pm$4.65	B.199	1.96	$\pm$0.28	0	$\pm$14	A
720	Bohlinia	MBA	Sq	OC	5.97	$\pm\ 0.80\times10^{16}$	A.127	34.64	$\pm$1.81	B.200	2.74	$\pm$0.56	17	$\pm$20	C
735	Marghanna	MBA	Ch	CM	2.15	$\pm\ 0.68\times10^{18}$		72.27	$\pm$2.22	B.201	10.87	$\pm$3.56	0	$\pm$32	✗
739	Mandeville	MBA	Xc	Mes	1.16	$\pm\ 1.07\times10^{18}$		105.53	$\pm$1.68	B.202	1.88	$\pm$1.74	55	$\pm$92	D
747	Winchester	MBA	B	CV	3.81	$\pm\ 2.22\times10^{18}$	A.128	170.07	$\pm$6.70	B.203	1.47	$\pm$0.87	47	$\pm$59	D
751	Faina	MBA	Ch	CM	3.27	$\pm\ 0.58\times10^{18}$	A.129	107.31	$\pm$1.48	B.204	5.05	$\pm$0.92	0	$\pm$18	B
758	Mancunia	MBA	X	CV	9.31	$\pm\ 0.80\times10^{17}$		87.08	$\pm$1.31	B.205	2.69	$\pm$0.26	3	$\pm$9	B
760	Massinga	MBA	S	OC	1.33	$\pm\ 1.32\times10^{18}$		70.82	$\pm$0.92	B.206	7.15	$\pm$7.10	0	$\pm$99	D
762	Pulcova	MBA	Cb	CM[1]	1.40	$\pm 0.10\times10^{18}$	A.130	138.40	$\pm$5.96	B.207	1.00	$\pm$0.14	55	$\pm$14	B
769	Tatjana	MBA		CM	6.31	$\pm\ 0.64\times10^{18}$		106.27	$\pm$4.02	B.208	10.03	$\pm$1.52	0	$\pm$15	✗
776	Berbericia	MBA	Cgh	CM	2.20	$\pm\ 2.71\times10^{18}$	A.131	152.29	$\pm$4.25	B.209	1.18	$\pm$1.46	47	$\pm\infty$	E
784	Pickeringia	MBA	C	CM	3.74	$\pm\ 0.32\times10^{18}$		82.52	$\pm$7.18	B.210	12.70	$\pm$3.49	0	$\pm$27	✗
786	Bredichina	MBA	C	CM	2.82	$\pm\ 2.79\times10^{18}$		98.34	$\pm$6.00	B.211	5.66	$\pm$5.69	0	$\pm\infty$	E
790	Pretoria	MBA	X	Cv	4.58	$\pm\ 0.28\times10^{18}$	A.132	160.98	$\pm$11.16	B.212	2.09	$\pm$0.45	24	$\pm$21	C
804	Hispania	MBA	C	CM	5.00	$\pm\ 1.78\times10^{18}$	A.133	148.25	$\pm$4.08	B.213	2.93	$\pm$1.06	0	$\pm$36	C
809	Lundia	MBA	V	HED	9.27	$\pm\ 3.09\times10^{14}$		10.26	$\pm$0.07		1.64	$\pm$0.10	49	$\pm$6	B
854	Frostia	MBA	V	HED	1.06	$\pm\ 0.95\times10^{15}$		8.39	$\pm$1.27	B.214	0.88	$\pm$0.13	72	$\pm$14	B
895	Helio	MBA	B	CV	9.87	$\pm\ 6.05\times10^{18}$	A.134	148.43	$\pm$5.02	B.215	5.76	$\pm$3.58	0	$\pm$62	D
914	Palisana	MBA	Ch	CM	2.35	$\pm\ 0.24\times10^{18}$		81.27	$\pm$5.34	B.216	8.36	$\pm$1.85	0	$\pm$22	✗
949	Hel	MBA	Xk	Mes	1.73	$\pm\ 0.62\times10^{18}$		63.56	$\pm$4.01	B.217	12.86	$\pm$5.19	0	$\pm$40	✗
1013	Tombecka	MBA	Xk	Mes	0.17	$\pm 1.43\times10^{18}$		35.18	$\pm$2.24	B.218	7.50	$\pm$62.74	0	$\pm\infty$	E
10^{15}	Christa	MBA	Xc	Mes	4.77	$\pm\ 0.68\times10^{18}$		99.77	$\pm$2.46	B.219	9.17	$\pm$1.46	0	$\pm$15	✗
10^{21}	Flammario	MBA	Cb	CM	5.14	$\pm\ 0.12\times10^{18}$		99.27	$\pm$3.27	B.220	10.03	$\pm$1.02	0	$\pm$10	✗
1036	Ganymed	NEA	S	OC	1.67	$\pm\ 3.18\times10^{17}$		34.28	$\pm$1.38	B.221	7.91	$\pm$15.10	0	$\pm\infty$	✗

Table 1 (*continued*)

Designation		Classification			Masses (kg)			Diameter (km)			Density		Porosity		Rank
#	Name	Dyn.	Tax.	Met.	M	δM	Fig.	ϕ	$\delta\phi$	Fig.	ρ	$\delta\rho$	$\mathcal{P}$	$\delta\mathcal{P}$	
1089	Tama	MBA	S	OC	8.90	$\pm$ 3.20×10^{14}		13.44	$\pm$0.61	B.222	2.52	$\pm$0.29	24	$\pm$11	B
1171	Rusthawelia	MBA	X	CV	1.81	$\pm$ 0.20×10^{18}		70.98	$\pm$2.42	B.223	9.66	$\pm$1.45	0	$\pm$15	✗
1313	Berna	MBA	S	OC	2.25	$\pm$ 2.00×10^{15}		13.93	$\pm$0.64	B.224	1.21	$\pm$0.14	63	$\pm$11	B
1669	Dagmar	MBA	ag	CM	3.98	$\pm$ 0.80×10^{16}	A.135	42.99	$\pm$2.86	B.225	0.95	$\pm$0.27	57	$\pm$28	C
1686	De Sitter	MBA		CM	6.76	$\pm$ 3.18×10^{18}		30.60	$\pm$1.41	B.226	450.51	$\pm$220.97	0	$\pm$49	✗
3169	Ostro	MBA	Xe	EH	1.86	$\pm$ 0.62×10^{14}		5.15	$\pm$0.08		2.59	$\pm$0.20	25	$\pm$7	B
3671	Dionysus	NEA	Cb	CM	8.38	$\pm$ 2.79×10^{11}		0.92	$\pm$0.05	B.227	1.60	$\pm$0.60	28	$\pm$37	C
3749	Balam	MBA	S	OC	5.09	$\pm$ 0.20×10^{14}		6.99	$\pm$3.00	B.228	2.83	$\pm$3.64	14	$\pm\infty$	E
4492	Debussy	MBA		CM	3.33	$\pm$ 3.00×10^{14}		15.78	$\pm$1.91	B.229	0.90	$\pm$0.10	60	$\pm$11	B
5381	Sekhmet	NEA	S	OC	1.04	$\pm$ 0.35×1012		1.00	$\pm$0.10		1.98	$\pm$0.65	40	$\pm$32	C
25143	Itokawa	NEA	S	OC	3.50	$\pm$ 0.10×1010		0.32	$\pm$0.01	B.230	1.91	$\pm$0.21	42	$\pm$11	A
26308	1998 SM165	TNO		Ice	6.78	$\pm$ 2.40×10^{18}		284.37	$\pm$5.07	B.231	0.56	$\pm$0.20	43	$\pm$35	C
35107	1991 VH	NEA	Sq	OC	1.40	$\pm$ 0.14×1012		1.13	$\pm$0.01	B.232	1.50	$\pm$0.50	54	$\pm$33	C
42355	Typhon	TNO		Ice	9.49	$\pm$ 0.52×10^{17}		181.70	$\pm$5.10	B.233	0.30	$\pm$0.03	69	$\pm$10	B
47171	1999 TC36	TNO		Ice	1.42	$\pm$ 0.02×10^{19}	A.136	402.46	$\pm$9.40	B.234	0.41	$\pm$0.03	58	$\pm$7	B
50000	Quaoar	TNO		Ice	1.60	$\pm$ 0.30×10^{21}		946.58	$\pm$137.26	B.235	3.60	$\pm$1.70	0	$\pm$47	C
58534	Logos	TNO		Ice	2.70	$\pm$ 0.30×10^{17}		110.00	$\pm$40.00		0.38	$\pm$0.42	61	$\pm\infty$	E
65489	Ceto	TNO		Ice	5.41	$\pm$ 0.42×10^{18}		250.58	$\pm$28.70	B.236	0.65	$\pm$0.23	34	$\pm$35	C
65803	Didymos	NEA		CM	5.24	$\pm$ 0.52×10^{11}		0.80	$\pm$0.08		1.90	$\pm$0.53	15	$\pm$28	C
66063	1998 RO1	NEA	S	OC	3.60	$\pm$ 1.80×10^{11}		0.68	$\pm$0.11	B.237	2.79	$\pm$1.47	15	$\pm$52	D
66391	1999 KW4	NEA	S	OC	2.35	$\pm$ 0.10×1012		1.31	$\pm$0.03		1.80	$\pm$0.29	45	$\pm$16	B
66652	Borasisi	TNO		Ice	3.75	$\pm$ 0.40×10^{18}		447.00	$\pm$90.00		0.08	$\pm$0.04	91	$\pm$61	D
88611	2001 QT297	TNO		Ice	2.36	$\pm$ 0.01×10^{18}	A.137	225.00	$\pm$75.00		0.39	$\pm$0.39	60	$\pm\infty$	E
90482	Orcus	TNO		Ice	6.34	$\pm$ 0.03×10^{20}	A.138	915.50	$\pm$42.58	B.238	1.57	$\pm$0.22	0	$\pm$13	B
134340	Pluto	TNO		Ice	1.30	$\pm$ 0.01×10^{22}		2390.00	$\pm$10.00		1.81	$\pm$0.02	0	$\pm$1	A
134860	2000 OJ67	TNO		Ice	2.14	$\pm$ 0.11×10^{18}		190.00	$\pm$65.00		0.59	$\pm$0.61	40	$\pm\infty$	E
136108	Haumea	TNO		Ice	4.01	$\pm$ 0.04×10^{21}	A.139	1244.99	$\pm$92.39	B.239	3.96	$\pm$0.88	0	$\pm$22	C
136199	Eris	TNO		Ice	1.66	$\pm$ 0.02×10^{22}		2357.83	$\pm$75.19	B.240	2.41	$\pm$0.23	0	$\pm$9	B
136617	1994 CC	NEA		CM	2.59	$\pm$ 0.13×10^{11}		0.62	$\pm$0.06		2.07	$\pm$0.61	7	$\pm$29	C
153591	2001 SN263	NEA		CM	9.17	$\pm$ 0.02×1012		2.59	$\pm$0.20		0.99	$\pm$0.22	55	$\pm$23	C
164121	2003 YT1	NEA		CM	1.27	$\pm$ 0.39×1012		1.08	$\pm$0.01	B.241	1.90	$\pm$0.59	15	$\pm$31	C
175706	1996 FG3	NEA	C	CM	4.27	$\pm$ 1.42×1012		1.75	$\pm$0.06	B.242	1.36	$\pm$0.65	39	$\pm$47	C
185851	2000 DP107	NEA		CM	4.60	$\pm$ 0.50×10^{11}		1.63	$\pm$0.35		0.95	$\pm$1.04	57	$\pm\infty$	E
276049	2002 CE26	NEA	C	CM	1.95	$\pm$ 0.25×10^{13}		3.46	$\pm$0.35		0.89	$\pm$0.29	60	$\pm$32	C
311066	2004 DC	NEA		CM	3.57	$\pm$ 0.36×1010		0.34	$\pm$0.03		1.73	$\pm$0.49	22	$\pm$28	C
1999	OJ4	TNO		Ice	3.91	$\pm$ 0.22×10^{17}		130.00	$\pm$45.00		0.33	$\pm$0.35	66	$\pm\infty$	E
2000	CF105	TNO		Ice	1.85	$\pm$ 0.12×10^{17}		188.00	$\pm$38.00		0.05	$\pm$0.03	94	$\pm$60	✗
2000	QL251	TNO		Ice	3.11	$\pm$ 0.05×10^{18}		150.00	$\pm$50.00		1.75	$\pm$1.76	0	$\pm\infty$	E
2000	UG11	NEA		CM	9.35	$\pm$ 1.59×10^{9}		0.30	$\pm$0.10		0.66	$\pm$0.67	70	$\pm\infty$	E
2001	QC298	TNO		Ice	1.08	$\pm$ 0.07×10^{19}		244.00	$\pm$55.00		1.41	$\pm$0.96	0	$\pm$67	D
2001	QW322	TNO		Ice	2.15	$\pm$ 0.18×10^{18}		128.00	$\pm$3.00		1.00	$\pm$1.00	0	$\pm\infty$	✗
2001	XR254	TNO		Ice	4.00	$\pm$ 0.17×10^{18}		225.00	$\pm$75.00		0.67	$\pm$0.67	32	$\pm\infty$	E
2003	QY90	TNO		Ice	1.01	$\pm$ 0.78×10^{18}		150.00	$\pm$50.00		0.57	$\pm$0.72	42	$\pm\infty$	E
2003	TJ58	TNO		Ice	2.25	$\pm$ 0.15×10^{17}		75.00	$\pm$25.00		1.01	$\pm$1.02	0	$\pm\infty$	E
2003	UN284	TNO		Ice	1.31	$\pm$ 0.26×10^{18}		124.00	$\pm$8.00		1.00	$\pm$1.00	0	$\pm\infty$	✗
2004	PB108	TNO		Ice	9.68	$\pm$ 0.57×10^{18}		140.00	$\pm$50.00		6.73	$\pm$7.22	0	$\pm\infty$	E
2005	EO304	TNO		Ice	2.10	$\pm$ 0.08×10^{18}		152.00	$\pm$2.00		1.00	$\pm$1.00	0	$\pm\infty$	✗
2006	BR284	TNO		Ice	5.70	$\pm$ 0.19×10^{17}		89.80	$\pm$0.90		1.00	$\pm$1.00	0	$\pm\infty$	✗
2006	JZ81	TNO		Ice	1.18	$\pm$ 0.51×10^{18}		122.00	$\pm$16.00		1.00	$\pm$1.00	0	$\pm\infty$	✗
2006	CH69	TNO		Ice	8.30	$\pm$ 2.75×10^{17}		99.99	$\pm$11.00		1.00	$\pm$1.00	0	$\pm\infty$	✗
2007	TY430	TNO		Ice	7.90	$\pm$ 2.10×10^{17}		50.00	$\pm$20.00		0.75	$\pm$1.00	25	$\pm\infty$	✗
	1P/Halley	COM		Ice	3.20	$\pm$ 1.20×10^{14}		10.39	$\pm$2.00		0.54	$\pm$0.37	45	$\pm$68	D
	2P/Encke	COM		Ice	9.20	$\pm$ 5.80×10^{13}		4.71	$\pm$0.81	B.243	1.67	$\pm$1.36	0	$\pm$81	D
	6P/dArest	COM		Ice	2.80	$\pm$ 0.80×10^{12}		1.70	$\pm$0.20		1.08	$\pm$0.49	0	$\pm$45	C

9P/Tempel1	COM	Ice	5.48	$\pm 0.56 \times 10^{13}$	A.140	6.00	$\pm$ 0.20	B.244	0.48	$\pm$ 0.06	51	$\pm$ 14	B
10P/Tempel2	COM	Ice	3.50	$\pm 1.50 \times 10^{14}$		9.60	$\pm$ 1.39		0.75	$\pm$ 0.46	24	$\pm$ 61	D
19P/Borrely	COM	Ice	2.70	$\pm 2.10 \times 10^{12}$		4.80	$\pm$ 0.40		0.12	$\pm$ 0.09	87	$\pm$ 77	✗
22P/Kopff	COM	Ice	5.30	$\pm 2.20 \times 10^{12}$		3.59	$\pm$ 0.40		0.21	$\pm$ 0.11	78	$\pm$ 53	D
45P/H-M-P	COM	Ice	1.90	$\pm 3.50 \times 10^{11}$		0.66	$\pm$ 0.20		1.26	$\pm$ 2.59	0	$\pm \infty$	E
46P/Wirtanen	COM	Ice	3.30	$\pm 2.30 \times 10^{11}$		1.15	$\pm$ 0.06		0.40	$\pm$ 0.28	59	$\pm$ 71	D
67P/C-G	COM	Ice	1.50	$\pm 0.60 \times 10^{13}$		2.96	$\pm$ 0.10	B.245	0.43	$\pm$ 0.37	56	$\pm$ 85	D
81P/Wild2	COM	Ice	8.10	$\pm 0.81 \times 10^{12}$		2.08	$\pm$ 0.06	B.246	0.10	$\pm$ 0.10	30	$\pm$ 14	B
SL9	COM	Ice	1.53	$\pm 0.15 \times 10^{12}$		1.79	$\pm$ 0.18		0.50	$\pm$ 0.05	50	$\pm$ 10	B

Table 2
Average bulk density (ρ) measured on $\mathcal{N}_s$ sample of $\mathcal{N}_m$ meteorites used in Table 1: Ordinary chondrites (OC: H, L, and LL), Carbonaceous chondrites (CC: CI, CM, CR, CO, CV, and CK), Enstatites chondrites (EH and EL), Achondrites HED (*i.e.*, average of Howardites, Eucrites, and Diogenites), Stony-Iron (Pallasites, Mesosiderites, and Steinbach), and Iron meteorites (Ataxites and Hexahedrites). Terrestrial weathering has a strong effect on the porosity of found OCs with respect to fallen OCs (Consolmagno et al., 2008). Only measurements on falls are therefore used here. For the other meteorite classes, both finds and falls are used. The density of liquid water of 1.00 ± 0.10 is used as a proxy for the volatiles that compose icy bodies. **References**: (1) Consolmagno and Britt (1998). (2) Britt and Consolmagno (2003), (3) Consolmagno et al. (2008), (4) Macke et al. (2010), and (5) Macke et al. (2011).

Meteorite		ρ	$\mathcal{N}_s$	$\mathcal{N}_m$	Refs.
Ord. chondrites	H	3.42 ± 0.18	265	157	2,3
Ord. chondrites	L	3.36 ± 0.16	277	160	2,3
Ord. chondrites	LL	3.22 ± 0.22	149	39	2,3
Carb. Chondrites	CI	1.60 ± 0.03	14	4	2,3
Carb. Chondrites	CM	2.25 ± 0.08	33	18	2,3
Carb. Chondrites	CR	3.10	7	3	2
Carb. Chondrites	CO	3.03 ± 0.19	22	8	2,3
Carb. Chondrites	CV	2.79 ± 0.06	51	10	2,3
Carb. Chondrites	CK	2.85 ± 0.08	3	3	3
Enstatites	EH	3.47 ± 0.21	16	9	4
Enstatites	EL	3.46 ± 0.32	25	14	4
Achondrites	HED	3.25 ± 0.26	96	56	5
Stony-Iron	Pal	4.76 ± 0.10	10	5	2
Stony-Iron	Mes	4.35 ± 0.02	8	3	2
Stony-Iron	Ste	4.18 ± 0.10	2	1	2
Iron	Ata	4.01 ± 0.04	1	1	1
Iron	Hex	7.37 ± 0.14	2	2	1
Iron	Oct	7.14 ± 0.13	5	5	1

relative accuracy better 20% only, the statistic is however based on low-numbers (see Table 3). The situation is particularly dramatic for end-members: only K-type and V-types have reliable estimates. The number of density estimates for comets and TNOs also drops with increasing levels of relative precision (Table 3).

The density estimates are plotted in Fig. 7, regrouped into six categories: TNOs, comets, and four asteroid groups: S-, C-, and X-complexes, and end-members. Macroporosity estimates (Eq. (2)) are similarly plotted in Fig. 8. Several trends can be observed:

- Asteroids in the S-complex are more dense than those in the C-complex (confirming Britt et al. (2002) findings).
- Asteroids in the C-complex seem to have larger macroporosity than those in the S-complex.
- The density of asteroids from both the S-complex and the C-complex seems to increase with the mass, apparently resulting from a decreasing macroporosity.
- In both C- and S-complexes, NEAs seem to have a lower density than MBAs, following the trend between mass and density observed for MBAs.
- At comparable sizes, B-types appear significantly denser ($\rho \sim 2.4$) than the other types of the C-complex that gather around $\rho \sim 1.4$.
- The density of the X-complex asteroids covers a large range, from the most dense Xc-types with $\rho \sim 4.9$ to X-types with $\rho \sim 1.8$.
- Comets have very low densities ($\rho \sim 0.5$), low even considering their volatile-rich composition (in agreement with spacecraft observations, see, Richardson et al., 2007).
- The density of TNOs covers a large range, from comet-like ($\rho \sim 0.5$) to the rocky (50 000) Quaoar ($\rho \sim 3.6$).
- Dwarf-planets apparently have no macroporosity, contrary to small bodies whose masses are inferior to $\approx 10^{20}$ kg.
- For each type of small body, the dispersion in density and macroporosity is huge.

Table 3
Average density ρ_i for each asteroid taxonomic type (DeMeo et al., 2009), based on $\mathcal{N}_i$ estimates. The i indices stand for the level of accuracy considered: more accurate than 20%, 50%, and no restriction on precision (∞). For each class, the associated meteorite (Met., see Table 2) and number of asteroids observed by DeMeo et al. (2009) with the corresponding fraction represented by the class are reported. The average density for transneptunian objects and comets are also reported.

Type	Met.	Taxonomy		Average density for each class					
		(#)	(%)	$\mathcal{N}_\infty$	ρ_∞	$\mathcal{N}_{50}$	ρ_{50}	$\mathcal{N}_{20}$	ρ_{20}
S	OC	144	38	50	2.66 ± 1.29	28	2.70 ± 0.69	11	2.72 ± 0.54
Sa	OC	2	<1	1	1.07 ± 0.25	1	1.07 ± 0.25		–
Sq	OC	29	7	5	2.78 ± 0.85	4	2.78 ± 0.81	2	3.43 ± 0.20
Sr	OC	22	5		–		–		–
Sv	OC	2	<1		–		–		–
B	CV	4	1	10	2.19 ± 1.00	4	2.15 ± 0.74	2	2.38 ± 0.45
C	CM	13	3	33	1.57 ± 1.38	19	1.41 ± 0.69	5	1.33 ± 0.58
Cb	CM	3	<1	13	1.88 ± 2.09	6	1.43 ± 0.74	3	1.25 ± 0.21
Cg	CM	1	<1	1	0.96 ± 0.27	1	0.96 ± 0.27		–
Cgh	CM	10	2	5	2.64 ± 1.35	1	3.48 ± 1.06		–
Ch	CM	18	4	47	1.96 ± 1.65	27	1.70 ± 1.10	9	1.41 ± 0.29
X	CV	4	1	26	2.87 ± 2.59	15	1.99 ± 0.99	8	1.85 ± 0.81
Xc	Mes	3	<1	9	4.96 ± 2.39	3	4.63 ± 0.76	2	4.86 ± 0.81
Xe	EH	7	1	4	2.94 ± 0.85	2	2.91 ± 0.65	1	2.60 ± 0.20
Xk	Mes	18	4	13	3.85 ± 1.27	9	3.79 ± 1.18	3	4.22 ± 0.65
D	CM	16	4	3	9.56 ± 0.22		–		–
K	CV	16	4	2	4.25 ± 2.03	1	3.54 ± 0.21	1	3.54 ± 0.21
L	CO	22	5	4	3.24 ± 1.03	3	3.22 ± 0.97		–
T	Ata	4	1	1	2.61 ± 2.54		–		–
A	Pal	6	1	1	3.73 ± 1.40	1	3.73 ± 1.40		–
O	OC	1	<1		–		–		–
Q	OC	8	2		–		–		–
R	OC	1	<1	1	2.23 ± 1.02	1	2.23 ± 1.02		–
V	HED	17	4	3	1.93 ± 1.07	3	1.93 ± 1.07	3	1.93 ± 1.07
Transneptunian objects				22	0.77 ± 0.80	10	1.06 ± 0.80	6	1.06 ± 0.75
Comets				12	0.47 ± 0.25	4	0.56 ± 0.14	3	0.54 ± 0.09

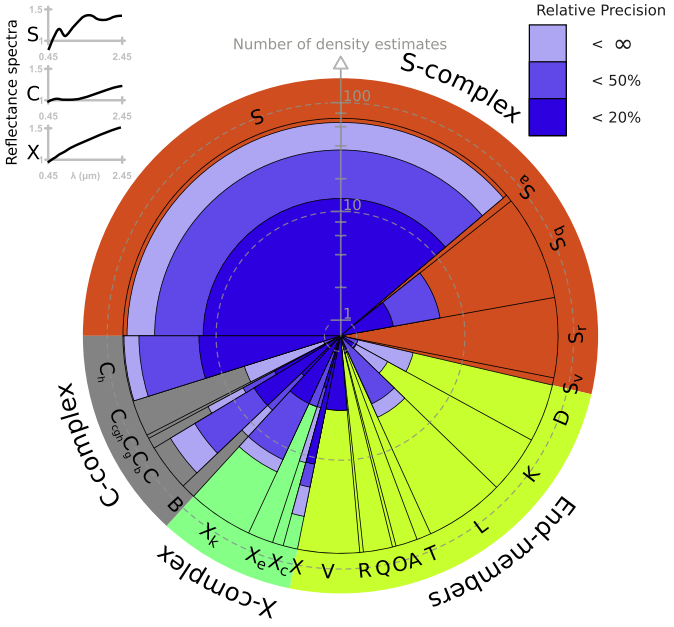

Fig. 6. Pie chart showing the fraction of asteroids within each class of the taxonomy by DeMeo et al. (2009), based on 371 objects. Complexes (C, S, and X) and end-members are displayed in gray, red, green and yellow respectively. Typical reflectance spectra of the complexes are also reported (top left). For each class, the number of density estimates, with a relative precision better than 20%, 50%, and regardless to the precision (∞), are drawn in blue wedges. (For interpretation of the references to color in this figure caption, the reader is referred to the web version of this article.)

These trends are discussed below. The large dispersion of values is however attributed to observational and methodological biases, rather than to genuine physical effects. Indeed, when considering different levels of accuracy, the distributions narrow with precision. In other words, biased estimates artificially spread the density distribution, hence the need for *realistic* evaluation of uncertainties.

5.1. C-complex and sub-groups

Most of the asteroids in the C-complex have densities ranging from the highly porous (253) Mathilde ($\rho \sim 1.3$) to the dense (2) Pallas ($\rho \sim 2.9$). This interval overlaps with CCs meteorites, and the structure of these asteroids ranges from large, compact, bodies ($\mathcal{P} \sim 0\%$) to rubble-piles ($\mathcal{P} \sim 40-60\%$). This trend for large bodies to present a zero macroporosity can be explained by the high pressure of their interiors. Following Britt et al. (2002), and references therein, silicate grains start to fracture when the pressure reaches $\sim 10^7$ Pa. This threshold is reached within the first few kilometers from the surface of large bodies, allowing a thin layer only to host macroporosity. Because large-scale *grains* (*i.e.*, rubble) are expected to grind at much smaller pressures, the transition from compact to fractured bodies is expected to be smooth.

Indeed, these different structures are apparently correlated with the mass of the asteroids (Fig. 9). The correlation coefficient between density and diameter is 68% and this trend seems real although the sample is still size-limited. From this trend (the linear regression in Fig. 9), the mass of hypothetical asteroids made of each type of CCs meteorites, without macroporosity, are all within $10^{19}-10^{20}$ kg, corresponding to the observed transition between compact and fractured asteroids. This suggests that large C-complex asteroids ($\phi \geq 300$ km) have intact structures, while smaller asteroids have porous interiors because the internal pressure never reaches the threshold for silicate compaction. This is consistent with the current vision of the dynamical history of the Main Belt: large asteroids survived intact throughout the history of the Solar System, while most of the material was removed or grinded into pieces (Morbidelli et al., 2009). This is

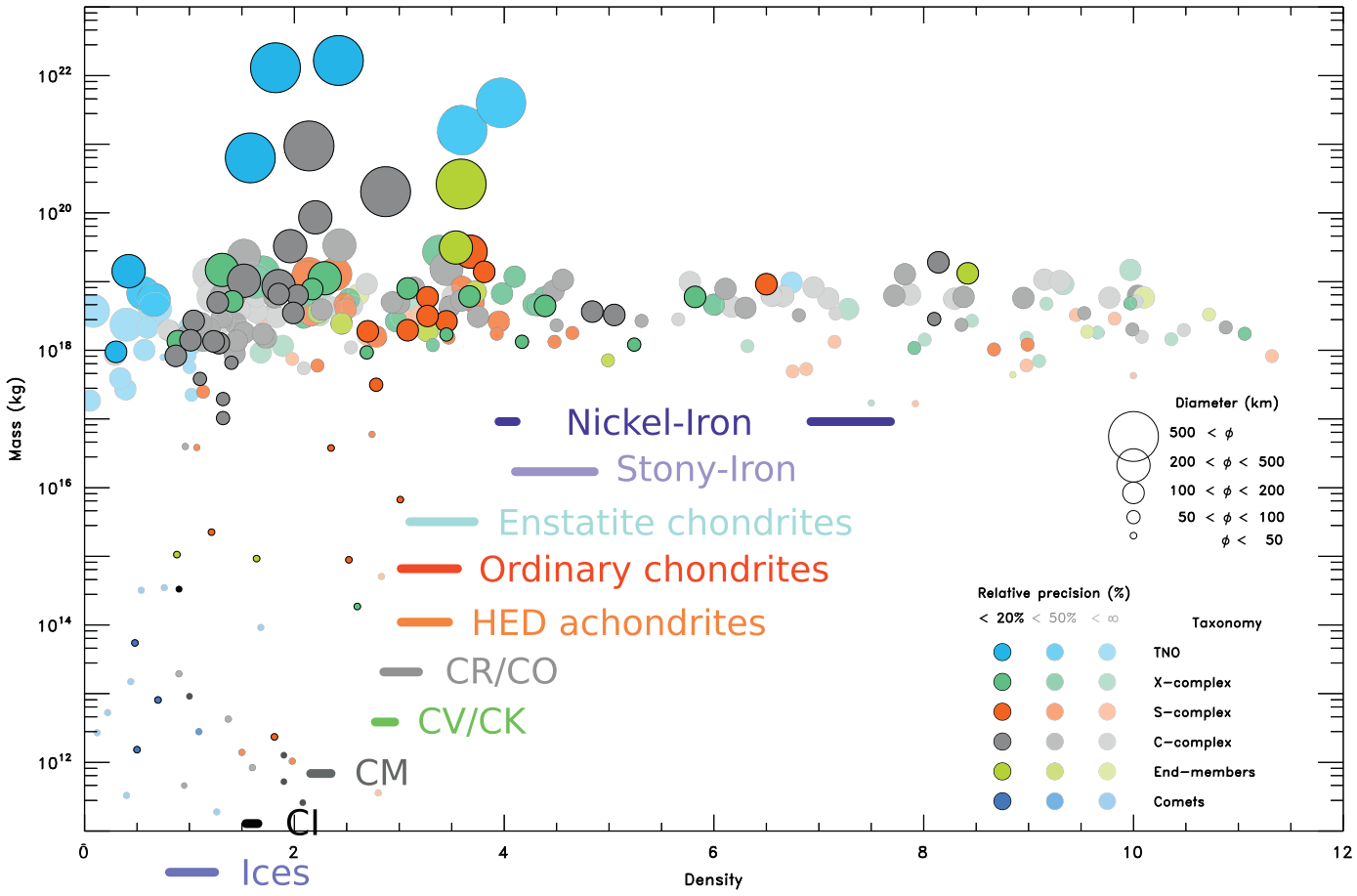

Fig. 7. Density vs. Mass. Small bodies are divided into six categories: TNOs (light blue), comets (blue), and asteroids (all dynamic class together) divided into four taxonomic groups: S-complex in red, C-complex in grey, X-complex in green, and end-members in yellow (similar to Fig. 6). Asteroids which taxonomy is unknown are plotted in black. The size of the symbols is a function of the object diameters, and the three different levels of contrast correspond to three cuts of relative accuracy: $<20\%$, $<50\%$, and regardless to the precision ($<\infty$). The density of the different class of meteorites is also drawn, at arbitrary masses (Table 2). (For interpretation of the references to color in this figure caption, the reader is referred to the web version of this article.)

also supported by the apparent lower density of about 1.2 for the 7 NEAs, with respect to about 2 for the 53 MBAs.

Among the C-complex, B-types have distinct surface properties: negative spectral slope in the visible and higher albedo (see the compilation of albedo per taxonomic class from Ryan and Woodward (2010); Usui et al. (2011); Masiero et al. (2011)). From a comprehensive comparison of 22 C-complex asteroids with laboratory spectra of meteorites, Clark et al. (2010) indeed found that spectra of C-types were best matched by aqueous-altered CI/CM carbonaceous chondrites while those of B-types by other CCs sub-groups (mainly CO, CV, but also CK and CR). This is supported by the density estimates (Table 3): B-types are significantly denser ($\rho \sim 2.4$) than the other types of the C-complex, following the trend observed in meteorites. Although only two B-types have density estimates more accurate than 20%, (2) Pallas and (704) Interamnia, this trend of a larger density is constantly found at different levels of precision (Table 3) and diameters (Table 1). B-types are thus intrinsically more dense than the other C-types, independently from the mass-density trend observed among C-complex asteroids (see above). Therefore, in addition to albedo and reflectance spectra that point toward different surface properties/composition, density suggests that there are fundamental differences in the composition and internal structures of B-types. The recent recovery of the Almahata Sitta meteorite, originating from the impact of asteroid 2008 TC_3 on Earth in October 2008, indeed indicated that B-type could be associated with unusual Ureilite achondrites (Jenniskens et al., 2009). Based on a comparison of the densities of (1) Ceres and (2) Pallas (used as archetypes for the definition of C and B taxonomic classes), Carry et al. (2010a) had suggested that B-types were less hydrated than C-types; a hypothesis supported by the lack of signature of organic or icy material in their spectra (Jones et al., 1990).

Finally, the three D-types have density estimates of around 9. These estimates were discarded from the analysis, as their uncertainty range does not overlap with meteorites, even the highly dense iron hexahedrites (Table 2).

5.2. S-complex and related end-members

The density of S-complex asteroids is distributed in a narrow interval (about 2 to 3), slightly below the density of their associated meteorites, the ordinary chondrites. The resulting macroporosity is generally smaller than 30%, *i.e.*, these asteroids may present cracks and fractures but are still coherent (not rubble-piles). This highlights intrinsic differences with the C-complex. The higher density is revelatory of the difference in composition: *basaltic* ordinary chondrites vs. *primitive* CI/CM carbonaceous chondrites. The lower macroporosity suggests a difference in formation and response to shocks. S-complex asteroids are made of *igneous* rocks, *i.e.*, they experienced a stage of high temperatures and were partly or entirely melted. If S-types acquired some cohesion in the process, subsequent impacts would have either not enough energy to overpass this cohesion barrier, leaving them with cracks and fractures only, or enough energy to break their

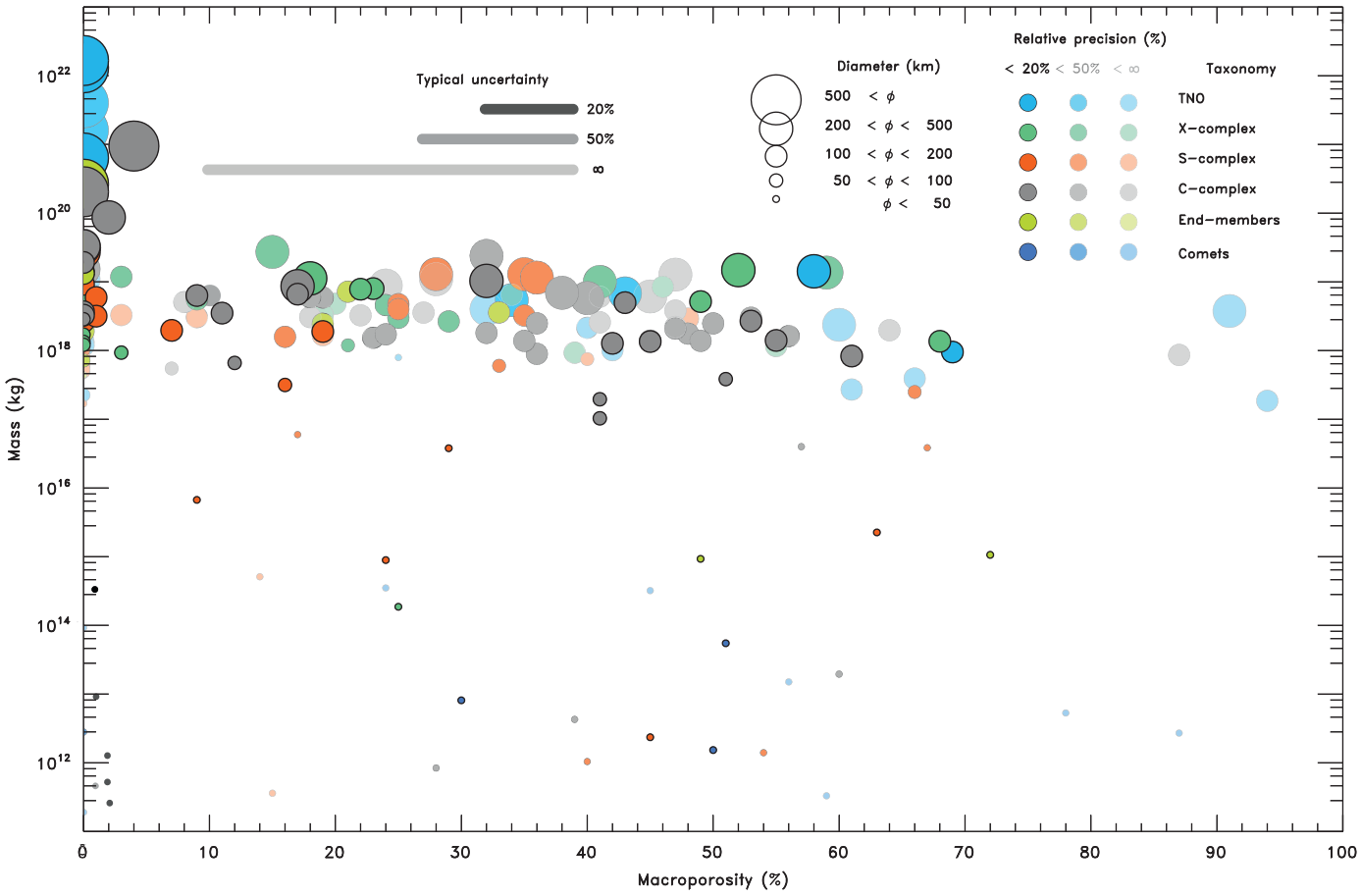

Fig. 8. Macroporosity vs. Mass. The color and size of the symbols are similar to Fig. 7. Macroporosity is obtained from Eq. (2) and the asteroid–meteorite links listed in Table 3. The typical uncertainty in macroporosity for three precision level on density are displayed (20%, 50%, and regardless to the precision: ∞). Additionally, an erroneous asteroid–meteorite link can shift any value by 30–40%. (For interpretation of the references to color in this figure caption, the reader is referred to the web version of this article.)

structure and destroy them ("battered to bits": Burbine et al. (1996)). The current S-complex asteroids would therefore be the few remnants of an originally much larger population (Morbidelli et al., 2009).

There are only four density estimates of asteroids belonging to the A and V classes. The only A-type, (354) Eleonora, has a density of 3.7 $\pm$1.4, much higher than S-types. This value is in agreement with the density of terrestrial olivines and stony-iron Pallasites meteorites (Section 2 and Table 2), although the rough relative accuracy allows a wide range of possibilities. Average density of the three V-types is surprisingly low: $\approx$1.9. A close inspection however reveals that (4) Vesta has a high density of 3.6 while the two 10 km-sized (809) Lundia and (854) Frostia have low densities of 1.6 and 0.9 respectively. These density measurements are hardly comparable. Vesta is a differentiated asteroid with a pyroxene-rich crust, analog to the HED meteorites, and a denser olivine-rich mantle (*e.g.*, McCord et al., 1970; Binzel et al., 1997). The low density of Lundia and Frostia implies a high macroporosity, above 50%, in the rubble-pile regime. Owing to their small size, they are the product of the collisional disruption of a larger parent body, and such a porous structure is not so surprising.

5.3. X-complex, or X melting pot?

The large spread in density and macroporosity of asteroids in the X-complex does not reduce with increasing levels of accuracy, contrary to the other groups of small bodies. This suggests that multiple compositions are present in the complex. This is supported by the many different proposed analog meteorites (see Section 2) and wider distribution of albedo with respect to C- and S-complexes (Figure 9 by Ryan and Woodward, 2010). The current definition of the X-complex (DeMeo et al., 2009) indeed encompass the former E, M, and P groups that were distinguished owing to their albedo (Tholen and Barucci, 1989).

Both Xc and Xk class have densities above 4, in the range of stony-iron and iron meteorites (Table 2). The density of X-types and Xe-types is lower, at about 1.8 and 2.6 respectively, closer to the proposed CV carbonaceous chondrites and enstatite chondrites meteorites. These asteroids have been grouped together in the taxonomy by DeMeo et al. (2009) owing to their spectra similarity. Given the low-contrast of their reflectance spectra, however, this grouping may be artificial. Many different compositions are likely to be represented among the X-complex. Further understanding and classification of these asteroids will benefit using a larger wavelength range (*e.g.*, Vernazza et al., 2011b) and albedo (*e.g.*, Ockert-Bell et al., 2010; Fornasier et al., 2011).

5.4. Dwarf-planets and small bodies

There are only eight small bodies more massive than 10^{20} kg: Ceres, Pallas, Vesta, Quaoar, Orcus, Pluto, Haumea, and Eris. These objects have diameters larger than 500 km and can be considered dwarf-planets. Their density is high, between 2 and 4, above that of their analog meteorites. This population particularly stands out in Fig. 8, where the dwarf-planets ($M \geq 10^{20}$ kg) are all packed near the $\mathcal{P} \approx 0$ axis, and the other small bodies below 10^{20} kg are

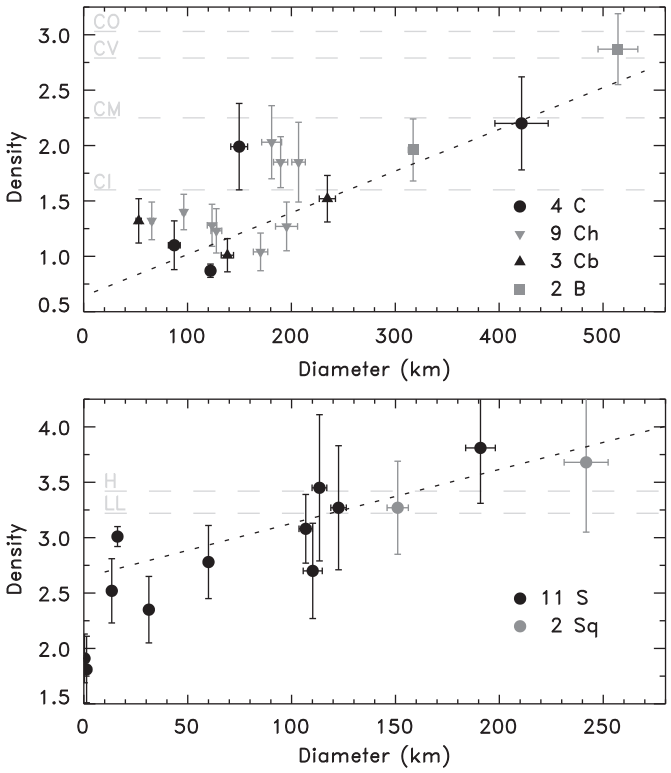

Fig. 9. Density *vs.* diameter. **Top:** The 18 asteroids in the C-complex (20% relative precision only, without Ceres). Average density for the CI, CM, CV, and CV carbonaceous chondrites is also reported (light grey horizontal dashed lines). The oblique dotted line is a linear regression on this sample with a correlation coefficient of 68%. **Bottom:** The 13 asteroids in the S-complex (20% relative precision only). Average density for the LL and H ordinary chondrites are also reported (light grey horizontal dashed lines). The oblique dotted line is a linear regression on this sample with a correlation coefficient of 51%.

spread over the entire graph. This suggests that these bodies are differentiated, with the presence of higher density material below the surface, *e.g.*, silicate or iron cores (Fraser and Brown, 2010; Castillo-Rogez and McCord, 2010).

The majority (75%) of the small bodies in the sample compiled here are main-belt and Trojan asteroids with masses between 10^{17} and 10^{20} kg. These asteroids have diameters between 50 and 400 km, densities between 0.9 and 5.8, and macroporosities up to 70%, from the highly porous (90) Antiope to the very compact asteroid (46) Hestia. The pressure inside an object with a mass lower than $\approx 10^{20}$ kg never reaches 10^7 Pa (the threshold for silicate grain compaction, see Section 5.1, Fig. 9, and Consolmagno et al., 2008). These high levels of macroporosity are therefore not unexpected. The broad range of densities is more surprising. It is partly due to different compositions of these objects, but also to the often large biases affecting the density estimates. Indeed, the fraction of asteroids with densities lower than 4 decreases from 56% to 16% by considering the estimates more precise than 20% only. Said differently, most of the small bodies with a density larger than ≈ 4 suffer from low-precision estimates with underestimated volume and/or overestimated mass.

This is supported by the distribution of density and macroporosity among NEAs ($M \leq 10^{17}$ kg). If the macroporosity of NEA also spans a similar range up to 70%, the most dense NEA is (433) Eros, with $\rho \sim 3$ *only*. By opposition to MBAs, all the mass estimates available for NEA were derived from a spacecraft encounter or from the orbit of a satellite, the most-precise techniques (Fig. 1). The accuracy on their density is therefore limited by the relative precision of their volume-equivalent diameters, which is generally less affected by biases (Section 4). The distribution of density among NEAs may therefore be more representative of the *real* density distribution than what we now observe for main-belt asteroids. Because NEAs only represent 6% of the sample presented here, strong efforts to improve the mass estimates of MBAs must be undertaken.

5.5. Transneptunian objects

This population includes a wide range of sizes, from dwarf-planets such as Pluto with diameters above 2000 km down to small bodies of a few tens of kilometers. All of the 28 TNOs listed in Table 1 have satellites and the main source of uncertainty is the precision on volume estimates, similar to NEAs. The situation is however worse for TNOs. Indeed, volume estimates from thermal radiometry (*e.g.*, Lellouch et al., 2010), stellar occultation (*e.g.*, Sicardy et al., 2011) or direct imaging (*e.g.*, Fraser and Brown, 2010) are available for the few larger TNOs only. The diameter of 11 TNOs was roughly estimated from their apparent magnitude. Given the lack of knowledge on their albedo and the 20% uncertainty affecting albedo estimates (see, Lim et al., 2010), only crude diameter estimates can be derived (Fig. 4a). The diameters of seven additional TNOs have been estimated from an *assumed* density of 1.0 (Parker et al., 2011; Sheppard et al., 2012). Only 10 density estimates were therefore determined from *direct* measurements. Of these, only five have a relative precision better than 20%: 1999 TC_{36}, Typhon, Orcus, Pluto, and Eris.

The five TNOs larger than ≈ 1000 km have densities above 1.5, indicating differentiated interiors as described before (Section 5.4). On the contrary, the five other 100 km-sized TNOs have densities around 0.5, indicative of highly porous structures ($\mathcal{P} \geq 50\%$). The increase in macroporosity for smaller objects is similar to that observed for asteroids. Current asteroid and TNO populations are the result of collisions over History and such similarities are therefore expected.

5.6. Comets

The comets are the least massive objects listed here, from 10^{14} to 10^{17} kg. With a diameter of typically a few hundred meters to a couple of kilometers and a very bright coma with respect to the nucleus itself as soon as they are active, observations of comet nuclei are very difficult. Current knowledge of the physical properties of comet nuclei is therefore still limited (Lamy et al., 2004).

The comets have a very low density: nine of the 12 comets listed here have a density below 1. The weighted average density of all 12 comets is 0.47 ± 0.25 only, marginally below the limit value of 0.6 inferred from rotation properties (*e.g.*, Lamy et al., 2004; Snodgrass et al., 2006). The resulting macroporosity is generally high ($\mathcal{P} \geq 30-50\%$), consistent with our current understanding of the structure of a comet nucleus: a highly porous assemblage of ices and silicates (see, Weissman et al., 2004, for a review). These values of density and macroporosity are consistent with those of the small-sized TNOs (Section 5.5). This is reassuring given that TNOs are thought to be the reservoir of Jupiter-family comets (Jewitt, 2004).

6. Perspectives

Our knowledge on the density and macroporosity of small bodies has seen a revolution in the last 10 years, from 17 objects listed by Britt et al. (2002), to 40 by Consolmagno et al. (2008), to 287 here. If the sample has increased by about an order of magnitude, only a third of the density estimates have a relative

precision better than 20%. Improving the accuracy of mass and volume estimates is therefore necessary. Several lines of investigations are still required to improve our understanding of asteroids composition and internal structure.

6.1. Asteroid-meteorite link

As briefly described in Section 2, only half of the 24 classes of the asteroid taxonomy have mineralogy interpretations (DeMeo et al., 2009). Together with the dynamic of asteroids, it is one of the fundamental knowledge required to constrain the models of planetary formation (*e.g.*, Morbidelli et al., 2005; Walsh et al., 2011). Efforts to determine the surface properties must be continued. Irradiation experiments in the laboratory have allowed to understand the space weathering processes on the surfaces of olivines- and pyroxenes-rich S-complex asteroids (see, Chapman, 1996; Strazzulla et al., 2005; Vernazza et al., 2006, 2009a, among many others), including the related end-members A- and V-types (Brunetto et al., 2007; Fulvio et al., 2012). The influence of the space weathering on the reflectance spectra of most meteorite types is however still unknown, apart from some experiments on enstatite chondrites and mesosiderites (Vernazza et al., 2009b).

Mid-infrared spectroscopy (2–5 and 5−40 μm range) will also help refining the mineralogy (*e.g.*, Rivkin et al., 2002; Emery et al., 2006), providing the regolith packing can be reproduced in the laboratory (*e.g.*, Vernazza et al., 2010, 2011a; King et al., 2011). Albedo measurements should also be used (Fornasier et al., 2011), although the typical uncertainty of about 20% that can be expected from simple thermal models (Lim et al., 2010) may preclude strong conclusions for the time being. Density can also greatly help in that respect. The comparison of bulk density resulting from the possible composition with the asteroid bulk density may confirm or invalidate the composition (Sierks et al., 2011). Refining the asteroid–meteorite links will allow to secure the macroporosity estimates, hence our knowledge of the interior of small bodies.

6.2. Accurate mass estimates

Estimating any mass at all is the limiting factor in determining the density of small bodies (*e.g.*, Consolmagno et al., 2008). Furthermore, in most of the cases, the density accuracy is hampered by the large uncertainty of mass estimates (Section 4.2). Improving the number and accuracy of mass estimates is therefore required.

The study of binary systems is highly relevant in that respect. It is the most productive method to determine accurate mass estimates (Fig. 1c). However, only a third of the 200 known binaries have a mass estimate (Section 4.1). Most of the binaries were indeed discovered from lightcurves, and their angular separation is too small to be resolved. Upcoming facilities such as the ALMA interferometer or the E-ELT will provide the angular resolution required to resolve these systems, and many more accurate mass determinations should be available in few years. Additional optical and radar imaging observations, together with lightcurves of mutual events of known binaries, will also help improving the current mass estimates (*e.g.*, Descamps et al., 2008).

In parallel, the astrometry observations by Gaia will provide additional mass determinations. Around 350 000 small bodies are expected to be observed during the 5 years mission, with an average of 50 to 60 epochs on each (Mignard et al., 2007). The micro-arcsecond precision of Gaia's astrometry will allow to refine the accuracy on the orbit of asteroids by several orders of magnitude. Such a precision will have a snowball effect on subsequent mass estimates from planetary ephemeris and orbit deflections. Close encounters between asteroids will also be observed during the mission and the mass of about 50 asteroids with an expected relative precision better than 10% will be determined (Mouret et al., 2007). Although most of these objects are most likely already listed in Appendix A, the mass estimates are expected to be less affected by biases, owing to the unprecedented completeness of Gaia catalog. The number of mass estimates and their level of accuracy is therefore expected to improve significantly at the 2020 horizon.

6.3. Accurate volume estimates

As described in Section 4, the contributions of the mass and diameter uncertainties to the density uncertainty are not even. The precision on the diameter is indeed the limiting factor of the most accurate density estimates (see also Fig. 3). Relative precision on the *volume* below 10–15% is required to take advantage of any mass determination. The accuracy on the *diameter* should therefore be of a few percent at most. Thanks to improved observing facilities and from improved methods of analysis, our understanding of the physical properties of asteroids as seen a revolution in last decade, making such a goal achievable.

Many different observing techniques and methods of analysis can be used to evaluate the diameter of small bodies. In particular, multi-data approaches have been proven successful in determining the 3-D shape, size, and spin axis of small bodies (see Section 4.2). The recent flyby of asteroid (21) Lutetia by the ESA Rosetta mission showed that the diameter estimate derived before the flyby from optical lightcurves and disk-resolved images was accurate to 2% (using the KOALA 3-D shape modeling algorithm, see, (Kaasalainen, 2011; Carry et al., 2010b, 2012). Besides, 3-D shape models offer the possibility to analyze thermal radiometry data with more advanced thermal models (*e.g.*, Lagerros, 1996, 1997; Müller et al., 2005; Mueller et al., 2006; Delbo and Tanga, 2009; Rozitis and Green, 2011; O'Rourke et al., 2012). Such models allow to derive several surface properties such as the albedo and thermal inertia. These quantities can in turn be used to help constraining the asteroid–meteorite links (Section 6.1). Large observing programs (*e.g.*, lightcurves, adaptive-optics disk-resolved images on large telescopes, stellar occultation campaigns) to derive 3-D shape models of all the small bodies listed in Table 1 have therefore far-reaching implications.

7. Conclusion

An extensive review of current knowledge on the density and macroporosity of small bodies is presented. The density estimates of 287 small bodies are presented, computed from 994 mass estimates, 1454 volume-equivalent diameter estimates, and 24 indirect density estimates. All the dynamical classes are represented in the sample: 17 near-Earth asteroids, 230 Main-Belt and Trojan asteroids, 12 comets, and 28 transneptunian objects. The accuracy and biases affecting mass and diameter estimates are discussed and best-estimates are strictly selected. Bulk densities are computed and compared with meteorite density, allowing to estimate the macroporosity. Although the sample still suffers from large uncertainties and often biases (Sections 4 and 5), several trends can be identified:

1. Dwarf-planets apparently have no macroporosity, contrary to small bodies whose mass is inferior to $\approx 10^{20}$ kg.
2. Asteroids in the S-complex are more dense than those in the C-complex that in turn present a larger macroporosity.

3. There is a trend of increasing density with mass for asteroids in both S- and C-complexes. This trends is also visible from the lower density of NEAs with respect to MBAs.
4. B-types seem structurally different from other C-complex asteroids (albedo, reflectance spectra, density).
5. The X-complex encompasses many different compositions and should be revised using additional data (*e.g.*, albedo).
6. Comets and TNOs have similar low density and high macroporosity, consistent with a structure of porous icy agglomerates.

Several lines of investigations to improve the number and accuracy of density estimates are discussed. The search for binary asteroids and subsequent orbital analysis, together with detailed 3-D shape modeling from multi-data inversion techniques stand out as key programs.

Acknowledgments

A big thank you to P. Tanga and D. Hestroffer for poking me about coming to the Gaia GREAT meeting in Pisa, without them I wouldn't have started this painful (but fruitful!) task of compiling masses. Dankeschön, merci to T. Müller, F. Marchis and A. Fienga for sharing their results ahead of publication. Thanks to F. DeMeo for constructive discussions. Thank you to the two anonymous referees for their constructive comments. As a result, the present manuscript includes a significantly higher amount of material in the introductory sections. Gracias R. Soja and E. Treguier for all our discussions about this topic and for the fun in the office. This research made heavy use of NASA's Astrophysics Data System Abstract Service (ADS) and Data Archive, thanks to the developers and maintainers.

Appendix A. Supplementary material

Supplementary data associated with this article can be found in the online version at doi:http://dx.doi.org.10.1016/j.pss.2012.03.009.

References

Baer, J., Chesley, S.R., 2008. Astrometric masses of 21 asteroids, and an integrated asteroid ephemeris. Celestial Mechanics and Dynamical Astronomy 100, 27–42.

Baer, J., Chesley, S.R., Matson, R.D., 2011. Astrometric masses of 26 asteroids and observations on asteroid porosity. Astronomical Journal 141, 143–155.

Baer, J., Milani, A., Chesley, S.R., Matson, R.D., 2008. An observational error model, and application to asteroid mass determination. Bulletin of the American Astronomical Society 141, 493.

Barucci, A., Belskaya, I., Fornasier, S., Fulchignoni, M., Clark, B.E., Coradini, A., Capaccioni, F., Dotto, E., Birlan, M., Leyrat, C., Sierks, H., Thomas, N., Vincent, J.B., 2012. Overview of Lutetia's surface composition. Planetary and Space Science 66 (1), 23–30.

Barucci, M.A., Brown, M.E., Emery, J.P., Merlin, F., 2008. Composition and surface properties of transneptunian objects and centaurs. The Solar System Beyond Neptune, 143–160.

Barucci, M.A., Fulchignoni, M., Fornasier, S., Dotto, E., Vernazza, P., Birlan, M., Binzel, R.P., Carvano, J.M., Merlin, F., Barbieri, C., Belskaya, I.N., 2005. Asteroid target selection for the new Rosetta mission baseline. 21 Lutetia and 2867 Steins. Astronomy and Astrophysics 430, 313–317.

Behrend, R., Bernasconi, L., Roy, R., Klotz, A., Colas, F., Antonini, P., Aoun, R., Augustesen, K., Barbotin, E., Berger, N., Berrouachdi, H., Brochard, E., Cazenave, A., Cavadore, C., Coloma, J., Cotrez, V., Deconihout, S., Demeautis, C., Dorseuil, J., Dubos, G., Durkee, R., Frappa, E., Hormuth, F., Itkonen, T., Jacques, C., Kurtze, L., Laffont, A., Lavayssière, M., Lecacheux, J., Leroy, A., Manzini, F., Masi, G., Matter, D., Michelsen, R., Nomen, J., Oksanen, A., Pääkkönen, P., Peyrot, A., Pimentel, E., Pray, D.P., Rinner, C., Sanchez, S., Sonnenberg, K., Sposetti, S., Starkey, D., Stoss, R., Teng, J.P., Vignand, M., Waelchli, N., 2006. Four new binary minor planets: (854) Frostia, (1089) Tama, (1313) Berna, (4492) Debussy. Astronomy and Astrophysics 446, 1177–1184.

Bell, J.F., Davis, D.R., Hartmann, W.K., Gaffey, M.J., 1989. Asteroids—The big picture. Asteroids II, 921–945.

Binzel, R.P., Gaffey, M.J., Thomas, P.C., Zellner, B.H., Storrs, A.D., Wells, E.N., 1997. Geologic mapping of Vesta from 1994 Hubble space telescope images. Icarus 128, 95–103.

Bottke Jr., W.F., Cellino, A., Paolicchi, P., Binzel, R.P., 2002a. An overview of the asteroids: the asteroids III perspective. Asteroids III, 3–15.

Bottke Jr., W.F., Nesvorný, D., Grimm, R.E., Morbidelli, A., O'Brien, D.P., 2006. Iron meteorites as remnants of planetesimals formed in the terrestrial planet region. Nature 439, 821–824.

Bottke Jr., W.F., Vokrouhlický, D., Rubincam, D.P., Broz, M., 2002b. The effect of Yarkovsky thermal forces on the dynamical evolution of asteroids and meteoroids. Asteroids, 395–408.

Britt, D.T., Bell, J.F., Haack, H., Scott, E.R.D., 1992. The reflectance spectrum of troilite and the T-type asteroids. Meteoritics 27, 207.

Britt, D.T., Consolmagno, G.J., 2003. Stony meteorite porosities and densities: a review of the data through 2001. Meteoritics and Planetary Science 38, 1161–1180.

Britt, D.T., Yeomans, D.K., Housen, K.R., Consolmagno, G.J., 2002. Asteroid density, porosity, and structure. Asteroids III 1, 485–500.

Brown, M.E., Bouchez, A.H., Rabinowitz, D.L., Sari, R., Trujillo, C.A., vanDam, M.A., Campbell, R.D., Chin, J.C.Y., Hartman, S.K., Johansson, E.M., Lafon, R.E., LeMignant, D., Stomski Jr., P.J., Summers, D.M., Wizinowich, P.L., 2005. Keck observatory laser guide star adaptive optics discovery and characterization of a satellite to the large Kuiper belt pbject 2003 EL_{61}. Astrophysical Journal 632, L45–L48.

Brown, M.E., Ragozzine, D., Stansberry, J., Fraser, W.C., 2010. The size, density, and formation of the Orcus–Vanth system in the Kuiper belt. Astronomical Journal 139, 2700–2705.

Brown, M.E., Schaller, E.L., Roe, H.G., Rabinowitz, D.L., Trujillo, C.A., 2006. Direct measurement of the size of 2003 UB313 from the Hubble space telescope. Astrophysical Journal 643, L61–L63.

Brown, M.E., Trujillo, C.A., 2004. Direct measurement of the size of the large Kuiper belt object (50000) Quaoar. Astronomical Journal 127, 2413–2417.

Brunetto, R., de León, J., Licandro, J., 2007. Testing space weathering models on A-type asteroid (1951) Lick. Astronomy and Astrophysics 472, 653–656.

Brunetto, R., Vernazza, P., Marchi, S., Birlan, M., Fulchignoni, M., Orofino, V., Strazzulla, G., 2006. Modeling asteroid surfaces from observations and irradiation experiments: the case of 832 Karin. Icarus 184, 327–337.

Burbine, T.H., Duffard, R., Buchanan, P.C., Cloutis, E.A., Binzel, R.P., 2011. Spectroscopy of O-type asteroids. In: Lunar and Planetary Institute Science Conference Abstracts, p. 2483.

Burbine, T.H., McCoy, T.J., Meibom, A., Gladman, B., Keil, K., 2002. Meteoritic parent bodies: their number and identification. Asteroids III, 653–667.

Burbine, T.H., Meibom, A., Binzel, R.P., 1996. Mantle material in the main belt: battered to bits? Meteoritics and Planetary Science 31, 607–620.

Bus, S.J., 1999. Compositional Structure in the Asteroid Belt: Results of a Spectroscopic Survey. Ph.D. Thesis, Massachusetts Institute of Technology.

Carry, B., Dumas, C., Kaasalainen, M., Berthier, J., Merline, W.J., Erard, S., Conrad, A.R., Drummond, J.D., Hestroffer, D., Fulchignoni, M., Fusco, T., 2010a. Physical properties of (2) Pallas. Icarus 205, 460–472.

Carry, B., Hestroffer, D., DeMeo, F.E., Thirouin, A., Berthier, J., Lacerda, P., Sicardy, B., Doressoundiram, A., Dumas, C., Farrelly, D., Müller, T.G., 2011. Integral-field spectroscopy of (90482) Orcus–Vanth. Astronomy and Astrophysics 534, A115.

Carry, B., Kaasalainen, M., Leyrat, C., Merline, W.J., Drummond, J.D., Conrad, A.R., Weaver, H.A., Tamblyn, P.M., Chapman, C.R., Dumas, C., Colas, F., Christou, J.C., Dotto, E., Perna, D., Fornasier, S., Bernasconi, L., Behrend, R., Vachier, F., Kryszczynska, A., Polinska, M., Fulchignoni, M., Roy, R., Naves, R., Poncy, R., Wiggins, P., 2010b. Physical properties of the ESA Rosetta target asteroid (21) Lutetia. II. Shape and flyby geometry. Astronomy and Astrophysics 523, A94.

Carry, B., Kaasalainen, M., Merline, W.J., Müller, T.G., Jorda, L., Drummond, J.D., Berthier, J., O'Rourke, L., Ďurech, J., Küppers, M., Conrad, A.R., Dumas, C., Sierks, H., the OSIRIS Team, 2012. KOALA shape modeling technique validated at (21) Lutetia by ESA Rosetta mission. Planetary and Space Science 66 (1), 200–212.

Castillo-Rogez, J.C., McCord, T.B., 2010. Ceres: evolution and present state constrained by shape data. Icarus 205, 443–459.

Chapman, C.R., 1996. S-type asteroids, ordinary chondrites, and space weathering: the evidence from Galileo's fly-bys of Gaspra and Ida. Meteoritics and Planetary Science 31, 699–725.

Clark, B.E., Bus, S.J., Rivkin, A.S., Shepard, M.K., Shah, S., 2004. Spectroscopy of X-type asteroids. Astronomical Journal 128, 3070–3081.

Clark, B.E., Ockert-Bell, M.E., Cloutis, E.A., Nesvorny, D., Mothé-Diniz, T., Bus, S.J., 2009. Spectroscopy of K-complex asteroids: parent bodies of carbonaceous meteorites? Icarus 202, 119–133.

Clark, B.E., Ziffer, J., Nesvorný, D., Campins, H., Rivkin, A.S., Hiroi, T., Barucci, M.A., Fulchignoni, M., Binzel, R.P., Fornasier, S., DeMeo, F., Ockert-Bell, M.E., Licandro, J., Mothé-Diniz, T., 2010. Spectroscopy of B-type asteroids: subgroups and meteorite analogs. Journal of Geophysical Research (Planets) 115, E06005.

Cloutis, E.A., Hiroi, T., Gaffey, M.J., Alexander, C.M.O., Mann, P., 2011a. Spectral reflectance properties of carbonaceous chondrites: 1. CI chondrites. Icarus 212, 180–209.

Cloutis, E.A., Hudon, P., Hiroi, T., Gaffey, M.J., Mann, P., 2011b. Spectral reflectance properties of carbonaceous chondrites: 2. CM chondrites. Icarus 216, 309–346.

Consolmagno, G., Britt, D., Macke, R., 2008. The significance of meteorite density and porosity. Chemie der Erde/Geochemistry 68, 1–29.

Consolmagno, G.J., Britt, D.T., 1998. The density and porosity of meteorites from the Vatican collection. Meteoritics and Planetary Science 33, 1231–1241.
Davidsson, B.J.R., Gutiérrez, P.J., 2004. Estimating the nucleus density of Comet 19P/Borrelly. Icarus 168, 392–408.
Davidsson, B.J.R., Gutiérrez, P.J., 2005. Nucleus properties of Comet 67P/Churyumov Gerasimenko estimated from non-gravitational force modeling. Icarus 176, 453–477.
Davidsson, B.J.R., Gutiérrez, P.J., 2006. Non-gravitational force modeling of Comet 81P/Wild 2.I. A nucleus bulk density estimate. Icarus 180, 224–242.
Davidsson, B.J.R., Gutiérrez, P.J., Rickman, H., 2007. Nucleus properties of Comet 9P/Tempel 1 estimated from non-gravitational force modeling. Icarus 187, 306–320.
de León, J., Duffard, R., Licandro, J., Lazzaro, D., 2004. Mineralogical characterization of A-type asteroid (1951) Lick. Astronomy and Astrophysics 422, L59–L62.
Delbo, M., Tanga, P., 2009. Thermal inertia of main belt asteroids smaller than 100 km from IRAS data. Planetary and Space Science 57, 259–265.
DeMeo, F.E., Binzel, R.P., Slivan, S.M., Bus, S.J., 2009. An extension of the Bus asteroid taxonomy into the near-infrared. Icarus 202, 160–180.
Descamps, P., Marchis, F., Michalowski, T., Vachier, F., Colas, F., Berthier, J., Assafin, M., Dunckel, P.B., Polinska, M., Pych, W., Hestroffer, D., Miller, K.P.M., Vieira-Martins, R., Birlan, M., Teng-Chuen-Yu, J.P., Peyrot, A., Payet, B., Dorseuil, J., Léonie, Y., Dijoux, T., 2007. Figure of the double Asteroid 90 Antiope from adaptive optics and lightcurve observations. Icarus 187, 482–499.
Descamps, P., Marchis, F., Pollock, J., Berthier, J., Vachier, F., Birlan, M., Kaasalainen, M., Harris, A.W., Wong, M.H., Romanishin, W.J., Cooper, E.M., Kettner, K.A., Wiggins, P., Kryszczynska, A., Polinska, M., Coliac, J.F., Devyatkin, A., Verestchagina, I., Gorshanov, D., 2008. New determination of the size and bulk density of the binary Asteroid 22 Kalliope from observations of mutual eclipses. Icarus 196, 578–600.
Doressoundiram, A., Barucci, M.A., Fulchignoni, M., Florczak, M., 1998. EOS Family: A Spectroscopic Study. Icarus 131, 15–31.
Drummond, J.D., Christou, J.C., Nelson, J., 2009. Triaxial ellipsoid dimensions and poles of asteroids from AO observations at the Keck-II telescope. Icarus 202, 147–159.
Drummond, J.D., Conrad, A., Merline, W.J., Carry, B., Chapman, C.R., Weaver, H.A., Tamblyn, P.M., Christou, J.C., Dumas, C., 2010. Physical properties of the ESA Rosetta target asteroid (21) Lutetia. I. The triaxial ellipsoid dimensions, rotational pole, and bulk density. Astronomy and Astrophysics 523, A93.
Dumas, C., Carry, B., Hestroffer, D., Merlin, F., 2011. High-contrast observations of (136108) Haumea. A crystalline water-ice multiple system. Astronomy and Astrophysics 528, A105.
Dunham, D.W., Herald, D., Frappa, E., Hayamizu, T., Talbot, J., Timerson, B., 2011. Asteroid Occultations. NASA Planetary Data System. EAR-A-3-RDR-OCCULTATIONS-V9.0.
Ďurech, J., Kaasalainen, M., Herald, D., Dunham, D., 2011. Combining asteroid models derived by lightcurve inversion with asteroidal occultation silhouettes. Icarus 214, 652–670.
Elkins-Tanton, L.T., Weiss, B.P., Zuber, M.T., 2011. Chondrites as samples of differentiated planetesimals. Earth and Planetary Science Letters 305, 1–10.
Emery, J.P., Burr, D.M., Cruikshank, D.P., 2011. Near-infrared spectroscopy of trojan asteroids: evidence for two compositional groups. Astronomical Journal 141, 25.
Emery, J.P., Cruikshank, D.P., van Cleve, J., 2006. Thermal emission spectroscopy (5.2 38 μm) of three trojan asteroids with the Spitzer Space Telescope: detection of fine-grained silicates. Icarus 182, 496–512.
Fang, J., Margot, J.L., Brozovic, M., Nolan, M.C., Benner, L.A.M., Taylor, P.A., 2011. Orbits of near-earth asteroid triples 2001 SN263 and 1994 CC: Properties, Origin, and Evolution. Astronomical Journal 141, 154–169.
Fienga, A., Laskar, J., Morley, T., Manche, H., Kuchynka, P., Le Poncin-Lafitte, C., Budnik, F., Gastineau, M., Somenzi, L., 2009. INPOP08, a 4-D planetary ephemeris: from asteroid and time-scale computations to ESA Mars Express and Venus Express contributions. Astronomy and Astrophysics 507, 1675–1686.
Fienga, A., Manche, H., Kuchynka, P., Laskar, J., Gastineau, M., 2010. INPOP10a. Scientific Notes.
Fienga, A., Manche, H., Laskar, J., Gastineau, M., 2008. INPOP06: a new numerical planetary ephemeris. Astronomy and Astrophysics 477, 315–327.
Folkner, W.M., Williams, J.G., Boggs, D.H., 2009. The planetary and lunar ephemeris de 421. IPN Progress Report 42, pp. 1–34.
Fornasier, S., Clark, B.E., Dotto, E., 2011. Spectroscopic survey of X-type asteroids. Icarus 214, 131–146.
Fraser, W.C., Brown, M.E., 2010. Quaoar: a rock in the Kuiper belt. Astrophysical Journal 714, 1547–1550.
Fujiwara, A., Kawaguchi, J., Yeomans, D.K., Abe, M., Mukai, T., Okada, T., Saito, J., Yano, H., Yoshikawa, M., Scheeres, D.J., Barnouin-Jha, O.S., Cheng, A.F., Demura, H., Gaskell, G.W., Hirata, N., Ikeda, H., Kominato, T., Miyamoto, H., Nakamura, R., Sasaki, S., Uesugi, K., 2006. The rubble-pile asteroid Itokawa as observed by Hayabusa. Science 312, 1330–1334.
Fulvio, D., Brunetto, R., Vernazza, P., Strazzulla, G., 2012. Space weathering of Vesta and V-type asteroids: new irradiation experiments on HED meteorites. Astronomy and Astrophysics 537, L11.
Gounelle, M., Morbidelli, A., Bland, P.A., Spurny, P., Young, E.D., Sephton, M., 2008. Meteorites from the outer solar system? The Solar System Beyond Neptune, 525–541.
Grundy, W.M., Noll, K.S., Buie, M.W., Benecchi, S.D., Stephens, D.C., Levison, H.F., 2009. Mutual orbits and masses of six transneptunian binaries. Icarus 200, 627–635.
Halliday, A.N., Kleine, T., 2006. Meteorites and the timing, mechanisms, and conditions of terrestrial planet accretion and early differentiation. Meteorites and the Early Solar System II, 775–801.
Harris, A.W., 1998. A thermal model for near-Earth asteroids. Icarus 131, 291–301.
Hilton, J.L., 2002. Asteroid masses and densities. Asteroids III, 103–112.
Jenniskens, P., Shaddad, M.H., Numan, D., Elsir, S., Kudoda, A.M., Zolensky, M.E., Le, L., Robinson, G.A., Friedrich, J.M., Rumble, D., Steele, A., Chesley, S.R., Fitzsimmons, A., Duddy, S., Hsieh, H.H., Ramsay, G., Brown, P.G., Edwards, W.N., Tagliaferri, E., Boslough, M.B., Spalding, R.E., Dantowitz, R., Kozubal, M., Pravec, P., Borovicka, J., Charvat, Z., Vaubaillon, J., Kuiper, J., Albers, J., Bishop, J.L., Mancinelli, R.L., Sandford, S.A., Milam, S.N., Nuevo, M., Worden, S.P., 2009. The impact and recovery of asteroid 2008 TC_3. Nature 458, 485–488, http://dx.doi.org/10.1038/nature07920.
Jewitt, D.C., 2004. From cradle to grave: the rise and demise of the comets, pp. 659–676.
Jones, T.D., Lebofsky, L.A., Lewis, J.S., Marley, M.S., 1990. The composition and origin of the C, P and D asteroids: water as tracer of thermal evolution in the outer belt. Icarus 88, 172–193.
Kaasalainen, M., 2011. Maximum compatibility estimates and shape reconstruction with boundary curves and volumes of generalized projections. Inverse Problems and Imaging 5, 37–57.
King, P.L., Izawa, M.R.M., Vernazza, P., McCutcheon, W.A., Berger, J.A., Dunn, T., 2011. Salt: a critical material to consider when exploring the solar system. Lunar and Planetary Institute Science Conference Abstracts 42, p. 1985.
Konopliv, A.S., Yoder, C.F., Standish, E.M., Yuan, D.N., Sjogren, W.L., 2006. A global solution for the Mars static and seasonal gravity, Mars orientation, Phobos and Deimos masses, and Mars ephemeris. Icarus 182, 23–50.
Krasinsky, G.A., Pitjeva, E.V., Vasiliev, M.V., Yagudina, E.I., 2001. Estimating masses of asteroids. In: Communications of IAA of RAS.
Lagerros, J.S.V., 1996. Thermal physics of asteroids. I. Effects of shape, heat conduction and beaming. Astronomy and Astrophysics 310, 1011–1020.
Lagerros, J.S.V., 1997. Thermal physics of asteroids. III. Irregular shapes and albedo variegations. Astronomy and Astrophysics 325, 1226–1236.
Lamy, P.L., Toth, I., Fernandez, Y.R., Weaver, H.A., 2004. The sizes, shapes, albedos, and colors of cometary nuclei. Comets II, 223–264.
Lebofsky, L.A., 1978. Asteroid 1 Ceres—evidence for water of hydration. Monthly Notices of the Royal Astronomical Society 182, 17–21.
Lebofsky, L.A., Sykes, M.V., Tedesco, E.F., Veeder, G.J., Matson, D.L., Brown, R.H., Gradie, J.C., Feierberg, M.A., Rudy, R.J., 1986. A refined 'standard' thermal model for asteroids based on observations of 1 Ceres and 2 Pallas. Icarus 68, 239–251.
Lellouch, E., Kiss, C., Santos-Sanz, P., Müller, T.G., Fornasier, S., Groussin, O., Lacerda, P., Ortiz, J.L., Thirouin, A., Delsanti, A., Duffard, R., Harris, A.W., Henry, F., Lim, T., Moreno, R., Mommert, M., Mueller, M., Protopapa, S., Stansberry, J., Trilling, D., Vilenius, E., Barucci, A., Crovisier, J., Doressoundiram, A., Dotto, E., Gutiérrez, P.J., Hainaut, O.R., Hartogh, P., Hestroffer, D., Horner, J., Jorda, L., Kidger, M., Lara, L.M., Rengel, M., Swinyard, B.M., Thomas, N., 2010. 'TNOs are cool': a survey of the trans-neptunian region. II. The thermal lightcurve of (136108) Haumea. Astronomy and Astrophysics 518, L147.
Levison, H.F., Bottke, W.F., Gounelle, M., Morbidelli, A., Nesvorný, D., Tsiganis, K., 2009. Contamination of the asteroid belt by primordial trans-Neptunian objects. Nature 460, 364–366.
Lim, T.L., Stansberry, J., Müller, T.G., Mueller, M., Lellouch, E., Kiss, C., Santos-Sanz, P., Vilenius, E., Protopapa, S., Moreno, R., Delsanti, A., Duffard, R., Fornasier, S., Groussin, O., Harris, A.W., Henry, F., Horner, J., Lacerda, P., Mommert, M., Ortiz, J.L., Rengel, M., Thirouin, A., Trilling, D., Barucci, A., Crovisier, J., Doressoundiram, A., Dotto, E., Gutiérrez Buenestado, P.J., Hainaut, O.R., Hartogh, P., Hestroffer, D., Kidger, M., Lara, L.M., Swinyard, B.M., Thomas, N., 2010. TNOs are Cool: a survey of the trans-Neptunian region. III. Thermophysical properties of 90482 Orcus and 136472 Makemake. Astronomy and Astrophysics 518, L148.
Macke, R.J., Britt, D.T., Consolmagno, G.J., 2011. Density, porosity, and magnetic susceptibility of achondritic meteorites. Meteoritics and Planetary Science 46, 311–326.
Macke, R.J., Consolmagno, G.J., Britt, D.T., Hutson, M.L., 2010. Enstatite chondrite density, magnetic susceptibility, and porosity. Meteoritics and Planetary Science 45, 1513–1526.
Marchis, F., Descamps, P., Baek, M., Harris, A.W., Kaasalainen, M., Berthier, J., Hestroffer, D., Vachier, F., 2008a. Main belt binary asteroidal systems with circular mutual orbits. Icarus 196, 97–118.
Marchis, F., Descamps, P., Berthier, J., Hestroffer, D., Vachier, F., Baek, M., Harris, A.W., Nesvorný, D., 2008b. Main belt binary asteroidal systems with eccentric mutual orbits. Icarus 195, 295–316.
Marchis, F., Hestroffer, D., Descamps, P., Berthier, J., Laver, C., de Pater, I., 2005. Mass and density of Asteroid 121 Hermione from an analysis of its companion orbit. Icarus 178, 450–464.
Marchis, F., Kaasalainen, M., Hom, E.F.Y., Berthier, J., Enriquez, J., Hestroffer, D., Le Mignant, D., de Pater, I., 2006. Shape, size and multiplicity of main-belt asteroids. Icarus 185, 39–63.
Margot, J.L., Nolan, M.C., Benner, L.A.M., Ostro, S.J., Jurgens, R.F., Giorgini, J.D., Slade, M.A., Campbell, D.B., 2002. Binary asteroids in the near-Earth object population. Science 296, 1445–1448.
Masiero, J.R., Mainzer, A.K., Grav, T., Bauer, J.M., Cutri, R.M., Dailey, J., Eisenhardt, P.R.M., McMillan, R.S., Spahr, T.B., Skrutskie, M.F., Tholen, D., Walker, R.G., Wright, E.L., DeBaun, E., Elsbury, D., Gautier IV, T., Gomillion, S., Wilkins, A.,

2011. Main belt asteroids with WISE/NEOWISE. I. Preliminary albedos and diameters. Astrophysical Journal 741, 68.
McCord, T.B., Adams, J.B., Johnson, T.V., 1970. Asteroid Vesta: spectral reflectivity and compositional implications. Science 168, 1445–1447.
Merline, W.J., Close, L.M., Dumas, C., Chapman, C.R., Roddier, F., Ménard, F., Slater, D.C., Duvert, G., Shelton, C., Morgan, T., 1999. Discovery of a moon orbiting the asteroid 45 Eugenia. Nature 401, 565–568.
Merline, W.J., Weidenschilling, S.J., Durda, D.D., Margot, J.L., Pravec, P., Storrs, A.D., 2002. Asteroids do have satellites. Asteroids III, 289–312.
Michalak, G., 2000. Determination of asteroid masses—I. (1) Ceres, (2) Pallas and (4) Vesta. Astronomy and Astrophysics 360, 363–374.
Michalak, G., 2001. Determination of asteroid masses. II. (6) Hebe, (10) Hygiea, (15) Eunomia, (52) Europa, (88) Thisbe, (444) Typtis, (511) Davida and (704) Interamnia. Astronomy and Astrophysics 374, 703–711.
Mignard, F., Cellino, A., Muinonen, K., Tanga, P., Delbo, M., Dell'Oro, A., Granvik, M., Hestroffer, D., Mouret, S., Thuillot, W., Virtanen, J., 2007. The Gaia mission: expected applications to asteroid science. Earth Moon and Planets 101, 97–125.
Morbidelli, A., Bottke, W.F., Nesvorný, D., Levison, H.F., 2009. Asteroids were born big. Icarus 204, 558–573.
Morbidelli, A., Levison, H.F., Tsiganis, K., Gomes, R., 2005. Chaotic capture of Jupiter's Trojan asteroids in the early Solar System. Nature 435, 462–465.
Mottola, S., Lahulla, F., 2000. Mutual eclipse events in asteroidal binary system 1996 FG_3: observations and a Numerical Model. Icarus 146, 556–567.
Mouret, S., Hestroffer, D., Mignard, F., 2007. Asteroid masses and improvement with GAIA. Astronomy and Astrophysics 472, 1017–1027.
Mouret, S., Simon, J.L., Mignard, F., Hestroffer, D., 2009. The list of asteroids perturbing the Mars orbit to be seen during future space missions. Astronomy and Astrophysics 508, 479–489.
Mueller, M., Delbo, M., Hora, J.L., Trilling, D.E., Bhattacharya, B., Bottke, W.F., Chesley, S., Emery, J.P., Fazio, G., Harris, A.W., Mainzer, A., Mommert, M., Penprase, B., Smith, H.A., Spahr, T.B., Stansberry, J.A., Thomas, C.A., 2011. ExploreNEOs. III. Physical characterization of 65 potential spacecraft target asteroids. Astronomical Journal 141, 109.
Mueller, M., Harris, A.W., Bus, S.J., Hora, J.L., Kassis, M., Adams, J.D., 2006. The size and albedo of Rosetta fly-by target 21 Lutetia from new IRTF measurements and thermal modeling. Astronomy and Astrophysics 447, 1153–1158.
Müller, T.G., Lellouch, E., Böhnhardt, H., Stansberry, J., Barucci, A., Crovisier, J., Delsanti, A., Doressoundiram, A., Dotto, E., Duffard, R., Fornasier, S., Groussin, O., Gutiérrez, P.J., Hainaut, O.R., Harris, A.W., Hartogh, P., Hestroffer, D., Horner, J., Jewitt, D.C., Kidger, M., Kiss, C., Lacerda, P., Lara, L.M., Lim, T., Mueller, M., Moreno, R., Ortiz, J.L., Rengel, M., Santos-Sanz, P., Swinyard, B., Thomas, N., Thirouin, A., Trilling, D., 2009. TNOs are cool: a survey of the transneptunian region. Earth Moon and Planets 105, 209–219.
Müller, T.G., Sekiguchi, T., Kaasalainen, M., Abe, M., Hasegawa, S., 2005. Thermal infrared observations of the Hayabusa spacecraft target asteroid 25143 Itokawa. Astronomy and Astrophysics 443, 347–355.
Ockert-Bell, M.E., Clark, B.E., Shepard, M.K., Isaacs, R.A., Cloutis, E.A., Fornasier, S., Bus, S.J., 2010. The composition of M-type asteroids: synthesis of spectroscopic and radar observations. Icarus 210, 674–692.
O'Rourke, L., Müller, T.G., Valtchanov, I., Altieri, B., Gonz Ailez-Garcia, B., Bhattacharya, B., Jorda, L., Carry, B., Küppers, M., Groussin, O., Altwegg, K., Barucci, A., Bockelée-Morvan, D., Crovisier, J., Dotto, E., Garcia-Lario, P., Kidger, M., Llorente, A., Llorente, R., Marstona, A.P., Sanchez Portal, M., Schulz, R., Sierra, M., Teyssiera, D., Vavreka, R., 2012. Thermal & shape properties of Asteroid (21) Lutetia from Herschel observations around the Rosetta flyby. Planetary and Space Science 66 (1), 192–199.
Ostro, S.J., Magri, C., Benner, L.A.M., Giorgini, J.D., Nolan, M.C., Hine, A.A., Busch, M.W., Margot, J.L., 2010. Radar imaging of asteroid 7 Iris. Icarus 207, 285–294.
Ostro, S.J., Margot, J.L., Benner, L.A.M., Giorgini, J.D., Scheeres, D.J., Fahnestock, E.G., Broschart, S.B., Bellerose, J., Nolan, M.C., Magri, C., Pravec, P., Scheirich, P., Rose, R., Jurgens, R.F., De Jong, E.M., Suzuki, S., 2006. Radar imaging of binary near-Earth asteroid (66391) 1999 KW4. Science 314, 1276–1280.
Parker, A.H., Kavelaars, J.J., Petit, J.M., Jones, L., Gladman, B., Parker, J., 2011. Characterization of seven ultra-wide trans-neptunian binaries. Astrophysical Journal 743, 1.
Pätzold, M., Andert, T., Asmar, S.W., Anderson, J.D., Barriot, J.P., Bird, M.K., Husler, B., Hahn, M., Tellmann, S., Sierks, H., Lamy, P., Weiss, B.P., 2011. Asteroid 21 Lutetia: low mass, high density. Science 334, 491.
Petit, J.M., Durda, D.D., Greenberg, R., Hurford, T.A., Geissler, P.E., 1997. The long-term dynamics of Dactyl's orbit. Icarus 130, 177–197.
Pitjeva, E.V., 2001. Progress in the determination of some astronomical constants from radiometric observations of planets and spacecraft. Astronomy and Astrophysics 371, 760–765.
Pravec, P., Harris, A.W., 2007. Binary asteroid population. 1. Angular momentum content. Icarus 190, 250–259.
Pravec, P., Harris, A.W., Michalowski, T., 2002. Asteroid rotations. Asteroids III, 113–122.
Pravec, P., Scheirich, P., Kušnirák, P., Šarounová, L., Mottola, S., Hahn, G., Brown, P.G., Esquerdo, G.A., Kaiser, N., Krzeminski, Z., Pray, D.P., Warner, B.D., Harris, A.W., Nolan, M.C., Howell, E.S., Benner, L.A.M., Margot, J.L., Galád, A., Holliday, W., Hicks, M.D., Krugly, Y.N., Tholen, D.J., Whiteley, R.J., Marchis, F., Degraff, D.R., Grauer, A., Larson, S., Velichko, F.P., Cooney, W.R., Stephens, R., Zhu, J., Kirsch, K., Dyvig, R., Snyder, L., Reddy, V., Moore, S., Gajdoš, Š., Világi, J., Masi, G., Higgins, D., Funkhouser, G., Knight, B., Slivan, S.M., Behrend, R., Grenon, M., Burki, G., Roy, R., Demeautis, C., Matter, D., Waelchli, N., Revaz, Y., Klotz, A., Rieugné, G., Thierry, P., Cotrez, V., Brunetto, L., Kober, G., 2006. Photometric survey of binary near-Earth asteroids. Icarus 181, 63–93.
Pravec, P., Vokrouhlický, D., Polishook, D., Scheeres, D.J., Harris, A.W., Galád, A., Vaduvescu, O., Pozo, F., Barr, A., Longa, P., Vachier, F., Colas, F., Pray, D.P., Pollock, J., Reichart, D., Ivarsen, K., Haislip, J., Lacluyze, A., Kušnirák, P., Henych, T., Marchis, F., Macomber, B., Jacobson, S.A., Krugly, Y.N., Sergeev, A.V., Leroy, A., 2010. Formation of asteroid pairs by rotational fission. Nature 466, 1085–1088.
Richardson, J.E., Melosh, H.J., Lisse, C.M., Carcich, B., 2007. A ballistics analysis of the Deep Impact ejecta plume: determining Comet Tempel 1's gravity, mass, and density. Icarus 190, 357–390.
Rivkin, A.S., Howell, E.S., Britt, D.T., Lebofsky, L.A., Nolan, M.C., Branston, D.D., 1995. Three-micron spectrometric survey of M- and E-class asteroids. Icarus 117, 90–100.
Rivkin, A.S., Howell, E.S., Vilas, F., Lebofsky, L.A., 2002. Hydrated minerals on asteroids: the astronomical record. Asteroids III, 235–253.
Rozitis, B., Green, S.F., 2011. Directional characteristics of thermal-infrared beaming from atmosphereless planetary surfaces—a new thermophysical model. Monthly Notices of the Royal Astronomical Society 415, 2042–2062.
Ryan, E.L., Woodward, C.E., 2010. Rectified asteroid albedos and diameters from IRAS and MSX Photometry Catalogs. Astronomical Journal 140, 933–943.
Scheirich, P., Pravec, P., 2009. Modeling of lightcurves of binary asteroids. Icarus 200, 531–547.
Schmidt, B.E., Thomas, P.C., Bauer, J.M., Li, J., McFadden, L.A., Mutchler, M.J., Radcliffe, S.C., Rivkin, A.S., Russell, C.T., Parker, J.W., Stern, S.A., 2009. The shape and surface variation of 2 Pallas from the Hubble space telescope. Science 326, 275–278.
Shepard, M.K., Margot, J.L., Magri, C., Nolan, M.C., Schlieder, J., Estes, B., Bus, S.J., Volquardsen, E.L., Rivkin, A.S., Benner, L.A.M., Giorgini, J.D., Ostro, S.J., Busch, M.W., 2006. Radar and infrared observations of binary near-Earth Asteroid 2002 CE26. Icarus 184, 198–210.
Sheppard, S.S., Ragozzine, D., Trujillo, C., 2012. 2007 TY430: A Cold Classical Kuiper belt type binary in the Plutino population. Astronomical Journal 143 (3), Article ID 58, http://dx.doi.org/10.1088/0004-6256/143/3/58.
Sicardy, B., Ortiz, J.L., Assafin, M., Jehin, E., Maury, A., Lellouch, E., Hutton, R.G., Braga-Ribas, F., Colas, F., Hestroffer, D., Lecacheux, J., Roques, F., Santos-Sanz, P., Widemann, T., Morales, N., Duffard, R., Thirouin, A., Castro-Tirado, A.J., Jelínek, M., Kubánek, P., Sota, A., Sánchez-Ramírez, R., Andrei, A.H., Camargo, J.I.B., da Silva Neto, D.N., Gomes, A.R., Martins, R.V., Gillon, M., Manfroid, J., Tozzi, G.P., Harlingten, C., Saravia, S., Behrend, R., Mottola, S., Melendo, E.G., Peris, V., Fabregat, J., Madiedo, J.M., Cuesta, L., Eibe, M.T., Ullán, A., Organero, F., Pastor, S., de Los Reyes, J.A., Pedraz, S., Castro, A., de La Cueva, I., Muler, G., Steele, I.A., 2011. A Pluto-like radius and a high albedo for the dwarf planet Eris from an occultation. Nature 478, 493–496.
Sierks, H., Lamy, P., Barbieri, C., Koschny, D., Rickman, H., Rodrigo, R., A'Hearn, M.F., Angrilli, F., Barucci, A., Bertaux, J.L., Bertini, I., Besse, S., Carry, B., Cremonese, G., Da Deppo, V., Davidsson, B., Debei, S., De Cecco, M., De Leon, J., Ferri, F., Fornasier, S., Fulle, M., Hviid, S.F., Gaskell, G.W., Groussin, O., Gutierrez, P.J., Jorda, L., Kaasalainen, M., Keller, H.U., Knollenberg, J., Kramm, J.R., Kührt, E., Küppers, M., Lara, L.M., Lazzarin, M., Leyrat, C., Lopez Moreno, J.L., Magrin, S., Marchi, S., Marzari, F., Massironi, M., Michalik, H., Moissl, R., Naletto, G., Preusker, F., Sabau, L., Sabolo, W., Scholten, F., Snodgrass, C., Thomas, N., Tubiana, C., Vernazza, P., Vincent, J.B., Wenzel, K.P., Andert, T., Pätzold, M., Weiss, B.P., 2011. Images of asteroid (21) Lutetia: a remnant planetesimal from the early Solar System. Science 334, 487–490.
Snodgrass, C., Lowry, S.C., Fitzsimmons, A., 2006. Photometry of cometary nuclei: rotation rates, colours and a comparison with Kuiper belt objects. Monthly Notices of the Royal Astronomical Society 373, 1590–1602.
Somenzi, L., Fienga, A., Laskar, J., Kuchynka, P., 2010. Determination of asteroid masses from their close encounters with Mars. Planetary and Space Science 58, 858–863.
Sosa, A., Fernández, J.A., 2009. Cometary masses derived from non-gravitational forces. Monthly Notices of the Royal Astronomical Society 393, 192–214.
Stansberry, J., Grundy, W., Brown, M.E., Cruikshank, D.P., Spencer, J.R., Trilling, D., Margot, J.L., 2008. Physical properties of Kuiper belt and centaur objects: constraints from the Spitzer space telescope. The Solar System Beyond Neptune, 161–179.
Strazzulla, G., Dotto, E., Binzel, R.P., Brunetto, R., Barucci, M.A., Blanco, A., Orofino, V., 2005. Spectral alteration of the Meteorite Epinal (H5) induced by heavy ion irradiation: a simulation of space weathering effects on near-Earth asteroids. Icarus 174, 31–35.
Sunshine, J.M., Connolly, H.C., McCoy, T.J., Bus, S.J., La Croix, L.M., 2008. Ancient asteroids enriched in refractory inclusions. Science 320, 514.
Tedesco, E.F., Noah, P.V., Noah, M.C., Price, S.D., 2002. The supplemental IRAS minor planet survey. Astronomical Journal 123, 1056–1085.
Tholen, D.J., Barucci, M.A., 1989. Asteroid taxonomy. Asteroids II, 298–315.
Thomas, P.C., Parker, J.W., McFadden, L.A., Russell, C.T., Stern, S.A., Sykes, M.V., Young, E.F., 2005. Differentiation of the asteroid Ceres as revealed by its shape. Nature 437, 224–226.
Tsiganis, K., Gomes, R., Morbidelli, A., Levison, H.F., 2005. Origin of the orbital architecture of the giant planets of the solar system. Nature 435, 459–461.
Usui, F., Kuroda, D., Müller, T.G., Hasegawa, S., Ishiguro, M., Ootsubo, T., Ishihara, D., Kataza, H., Takita, S., Oyabu, S., Ueno, M., Matsuhara, H., Onaka, T., 2011. Asteroid catalog using Akari: AKARI/IRC mid-infrared asteroid survey. Publications of the Astronomical Society of Japan 63, 1117–1138.

Vernazza, P., Binzel, R.P., Rossi, A., Fulchignoni, M., Birlan, M., 2009a. Solar wind as the origin of rapid reddening of asteroid surfaces. Nature 458, 993–995.
Vernazza, P., Binzel, R.P., Thomas, C.A., DeMeo, F.E., Bus, S.J., Rivkin, A.S., Tokunaga, A.T., 2008. Compositional differences between meteorites and near-Earth asteroids. Nature 454, 858–860.
Vernazza, P., Brunetto, R., Binzel, R.P., Perron, C., Fulvio, D., Strazzulla, G., Fulchignoni, M., 2009b. Plausible parent bodies for enstatite chondrites and mesosiderites: Implications for Lutetia's fly-by. Icarus 202, 477–486.
Vernazza, P., Brunetto, R., Strazzulla, G., Fulchignoni, M., Rochette, P., Meyer-Vernet, N., Zouganelis, I., 2006. Asteroid colors: a novel tool for magnetic field detection? The case of Vesta. Astronomy and Astrophysics 451, 43–46.
Vernazza, P., Carry, B., Emery, J.P., Hora, J.L., Cruikshank, D.P., Binzel, R.P., Jackson, J., Helbert, J., Maturilli, A., 2010. Mid-infrared spectral variability for compositionally similar asteroids: implications for asteroid particle size distributions. Icarus 207, 800–809.
Vernazza, P., King, P.L., Izawa, M.R.M., Maturilli, A., Helbert, J., Cruikshank, D., Brunetto, R., Marchis, F., Binzel, R.P., Flemming, R.L., 2011a. Opening the mid-IR window on asteroid physical properties. In: Lunar and Planetary Institute Science Conference Abstracts, vol. 42, p. 1344.
Vernazza, P., Lamy, P., Groussin, O., Hiroi, T., Jorda, L., King, P.L., Izawa, M.R.M., Marchis, F., Birlan, M., Brunetto, R., 2011b. Asteroid (21) Lutetia as a remnant of earth's precursor planetesimals. Icarus 216, 650–659.
Veverka, J., Robinson, M., Thomas, P., Murchie, S., Bell, J.F., Izenberg, N., Chapman, C., Harch, A., Bell, M., Carcich, B., Cheng, A., Clark, B., Domingue, D., Dunham, D., Farquhar, R., Gaffey, M.J., Hawkins, E., Joseph, J., Kirk, R., Li, H., Lucey, P., Malin, M., Martin, P., McFadden, L., Merline, W.J., Miller, J.K., Owen, W.M., Peterson, C., Prockter, L., Warren, J., Wellnitz, D., Williams, B.G., Yeomans, D.K., 2000. NEAR at eros: imaging and spectral results. Science 289, 2088–2097.
Walsh, K.J., Morbidelli, A., Raymond, S.N., O'Brien, D.P., Mandell, A.M., 2011. A low mass for Mars from Jupiter's early gas-driven migration. Nature 475, 206–209.
Walsh, K.J., Richardson, D.C., Michel, P., 2008. Rotational breakup as the origin of small binary asteroids. Nature 454, 188–191.
Weisberg, M.K., McCoy, T.J., Krot, A.N., 2006. Systematics and evaluation of meteorite classification. Meteorites and the Early Solar System II, 19–52.
Weissman, P.R., Asphaug, E., Lowry, S.C., 2004. Structure and density of cometary nuclei. Comets II, 337–357.
Yeomans, D.K., Antreasian, P.G., Barriot, J.P., Chesley, S.R., Dunham, D.W., Farquhar, R.W., Giorgini, J.D., Helfrich, C.E., Konopliv, A.S., McAdams, J.V., Miller, J.K., Owen, W.M., Scheeres, D.J., Thomas, P.C., Veverka, J., Williams, B.G., 2000. Radio science results during the NEAR-shoemaker spacecraft rendezvous with eros. Science 289, 2085–2088.
Yeomans, D.K., Barriot, J.P., Dunham, D.W., Farquhar, R.W., Giorgini, J.D., Helfrich, C.E., Konopliv, A.S., McAdams, J.V., Miller, J.K., Owen Jr., W.M., Scheeres, D.J., Synnott, S.P., Williams, B.G., 1997. Estimating the mass of asteroid 253 Mathilde from tracking data during the NEAR flyby. Science 278, 2106.
Yurimoto, H., Abe, K.i., Abe, M., Ebihara, M., Fujimura, A., Hashiguchi, M., Hashizume, K., Ireland, T.R., Itoh, S., Katayama, J., Kato, C., Kawaguchi, J., Kawasaki, N., Kitajima, F., Kobayashi, S., Meike, T., Mukai, T., Nagao, K., Nakamura, T., Naraoka, H., Noguchi, T., Okazaki, R., Park, C., Sakamoto, N., Seto, Y., Takei, M., Tsuchiyama, A., Uesugi, M., Wakaki, S., Yada, T., Yamamoto, K., Yoshikawa, M., Zolensky, M.E., 2011. Oxygen isotopic compositions of asteroidal materials returned from Itokawa by the Hayabusa mission. Science 333, 1116–1118.
Zielenbach, W., 2011. Mass Determination Studies of 104 Large Asteroids. Astronomical Journal 142, 120–128.